



Low-temperature conversion of phenol into CO, CO₂ and H₂ by steam reforming over La-containing supported Rh catalysts

Domna A. Constantinou^a, M. Consuelo Álvarez-Galván^b, José Luis G. Fierro^b, Angelos M. Efstathiou^{a,*}

^a Heterogeneous Catalysis Laboratory, Department of Chemistry, University of Cyprus, University Campus, CY 1678 Nicosia, Cyprus

^b Instituto de Catálisis y Petroleoquímica, CSIS, C/Marie Curie 2, Cantoblanco, 28049 Madrid, Spain

ARTICLE INFO

Article history:

Received 12 August 2011

Received in revised form

26 December 2011

Accepted 3 January 2012

Available online 11 January 2012

Keywords:

Phenol steam reforming

Hydrogen production

Supported-Rh catalysts

HRTEM

XPS

CO₂-TPD

CO-TPD

CO₂-DRIFTS

H₂O-DRIFTS

Operando DRIFTS-mass spectrometry WGS

ABSTRACT

The steam reforming of phenol in the low-temperature range of 350–550 °C was studied over 0.5 wt% Rh supported on Ce_{0.15}Zr_{0.85}O₂, Zr_{0.93}La_{0.07}O₂, and Ce_{0.13}Zr_{0.83}La_{0.04}O₂ mixed metal oxides. The reforming specific activity (per gram of catalyst basis) was found to depend on (a) Rh dispersion, (b) the concentration (μmol g⁻¹) of labile oxygen species of support, as determined by “oxygen storage capacity” measurements, and (c) the promotion of the water–gas shift (WGS) reaction rate, all of which largely influenced by the support chemical composition. The addition of 4 atom% La³⁺ into the Ce_{0.15}Zr_{0.85}O₂ crystal structure was found to largely promote the dispersion of Rh, to increase significantly (by a factor of 1.75) the concentration of surface basic sites (μmol m⁻²) of Ce_{0.13}Zr_{0.83}La_{0.04}O₂ compared to Ce_{0.15}Zr_{0.85}O₂ support, to prevent to a large extent the inhibiting role of hydrogen in the rate of WGS reaction, and to influence significantly the concentration and structure of surface reaction intermediates of the WGS, namely: formate (HCOO⁻) and –OH groups formed on the support, and adsorbed CO formed on the Rh metal. The 0.5 wt% Rh/Ce_{0.13}Zr_{0.83}La_{0.04}O₂ catalyst led to a significantly better performance towards steam reforming of phenol in terms of phenol conversion, H₂-yield, and CO/CO₂ product ratio in the 350–450 °C range compared to a commercial Ni-based catalyst (44 wt% Ni) used for steam reforming reactions. At 400 °C, the 0.5 wt% Rh/Ce_{0.13}Zr_{0.83}La_{0.04}O₂ catalyst exhibited approximately 54% and 50%, respectively, higher phenol conversion and hydrogen yield, compared to the Ni-based industrial catalyst. The significantly lower CO/CO₂ product ratio obtained in the case of Rh/Ce_{0.13}Zr_{0.83}La_{0.04}O₂ compared to that obtained in the other supported-Rh catalysts is in agreement with the higher kinetic rate for the WGS reaction observed in the former catalyst.

© 2012 Elsevier B.V. All rights reserved.

1. Introduction

The increasing energy dependence on fossil fuels and their adverse impact on our planet's ecosystem could be considered as one of today's very important energy topics [1]. In response to this, continuing efforts are being made in the exploration of clean and renewable energy alternatives for sustainable development. One example, where catalysis plays a very important role, is the exploitation of carbon-neutral energy resources, such as bio-fuels, that is, fuels produced from renewable bio-feedstocks or biomass [2]. Molecular hydrogen has been identified as an ideal burning fuel that can be well suited for this purpose due to its potentially higher energy efficiency and lower formation of pollutants, in general, compared to any other fuel [3]. However, major technical hurdles remain along the pathway to market acceptance of H₂ as a major energy source [4]. For example, hydrogen purification,

low-cost and long-lived hydrogen fuel cells, high NO_x emissions when H₂ is used in internal combustion engines, H₂ delivery and storage infrastructures [4,5].

Since biomass is abundant, CO₂-neutral, and a renewable primary energy source, its conversion into hydrogen appears as a very promising and attractive approach [2,6]. The production of “bio-syngas” (mixture of mainly CH₄, H₂, CO and CO₂ gases) for power generation and chemicals, following catalytic steam gasification of biomass, appears to be one of the main efforts for meeting the goal for a biomass-based energy technology [7,8]. One of the biggest obstacles associated with the practical end-use application of the resulting biomass-derived raw “bio-syngas” is the formation of tars [7b,9,10]. Tars generally comprise the condensable fraction of organic gasification products, largely consisting of aromatics and oxygen-containing hydrocarbons with molecular weight higher than that of benzene. The presence of tars can lead to a number of process problems, including: blockage of gas engines and turbines, clog of fuel lines, catalysts coking, wastewater disposal problems, and increase of maintenance costs [9,10]. It was reported that addition of steam and the use of favourable

* Corresponding author. Tel.: +357 22 892776; fax: +357 22 892801.

E-mail address: efstath@ucy.ac.cy (A.M. Efstathiou).

gasification temperatures lower than 800 °C promote the production of oxygen-containing compounds, such as phenol [11,12], especially after following wood-gasification by steam in a fluidized bed reactor in the 600–700 °C range and at 1 atm [12].

Phenol is known as precursor of naphthalene formation, which is one of the most problematic tertiary tars molecules [13,14] causing corrosion in the internal combustion engines, contaminating significantly the waste-water derived from biomass gasifiers, and, therefore, imposing a costly waste-water treatment [14]. The use of an effective *in situ* conditioning process of “bio-syngas” for phenol removal is expected to improve the viability and efficiency of biomass gasification processes [13,14]. Catalytic steam reforming is an attractive proposal for the conversion of phenol into similar gas constituents found in the “bio-syngas” [15,16].

Nickel-based catalysts were found to be very effective in producing high yields of synthesis gas (CO/H₂) *via* steam reforming of hydrocarbons, including natural gas [7]. However, toxicity and deactivation problems caused by nickel, the latter due to a high built-up of surface carbon deposits, necessitates the development of new low-cost solid catalysts having comparable activity to nickel-based ones currently used [17]. In fact, supported-Ru and -Rh catalysts were shown to retard coke formation during steam reforming reactions [17,18], whereas alkaline and lanthanide metal oxides used in the catalyst carrier were also found to increase the rate of carbon gasification [17,19]. Supported-Rh catalysts have also been investigated towards bio-ethanol steam reforming [20]. In several cases the support chemical composition was reported to play a significant role in the overall activity and H₂ selectivity of reaction. In terms of hydrogen production and long term stability, MgO, CeO₂ and La₂O₃ were considered suitable supports for Rh due to their basic character [20]. Diagne et al. [21,22] studied a 2 wt% Rh supported on CeO₂, ZrO₂ and CeO₂-ZrO₂, where the latter support was found more effective for bio-ethanol steam reforming. Also, Rioche et al. [23] have investigated 1 wt% Rh/Ce_{0.5}Zr_{0.5}O₂ and 1 wt% Rh/Al₂O₃ catalysts for the steam reforming of phenol and bio-oil. In the case of 1 wt% Rh/Ce_{0.5}Zr_{0.5}O₂ catalyst, the main products formed were CO₂ and H₂, with only small yields towards CO and CH₄ formation. Based on the H₂-yield, Ce_{0.5}Zr_{0.5}O₂ support proved to be more efficient than alumina. Montini et al. [24] have proposed a procedure to prepare active and stable (prevention of coke deposition and sintering of the active phase) Rh/Ce_xZr_{1-x}O₂/Al₂O₃ nanocomposites for efficient hydrogen production *via* steam reforming of ethanol. In addition, Asadullah et al. [25,26,27,28] developed supported-Rh catalysts based on CeO₂ and CeO₂/SiO₂, where the low-temperature gasification of cellulose and biomass was significantly enhanced.

The use of supported-Rh catalysts towards the selective conversion of phenol into H₂, CO and CO₂ by steam reforming in the low-temperature range of 350–550 °C [29] and at higher temperatures (575–730 °C) [30,31,32] was recently studied in our laboratory. Based on these studies, Rh-based catalysts could be considered as potential industrial catalytic systems for “bio-syngas” purification from tars in fixed-bed reactor configurations, where low loadings of Rh (less than about 0.5 wt%) and reaction temperatures of less than 500 °C could be seen as realistic conditions to reduce investment and operational costs.

The present work is a continuation of our previous works reported [29,30,31,32], and is focused on the study of steam reforming of phenol in the low-temperature range of 350–550 °C over 0.5 wt% Rh supported on Ce–Zr–La–O mixed metal oxides. In an effort to develop relationships between important surface/bulk physico-chemical and catalytic performance properties, various bulk and surface characterization techniques were used, namely: BET, X-ray diffraction, HR-TEM, XPS, H₂, CO₂, and CO temperature-programmed desorption (TPD), H₂ temperature-programmed reduction (H₂-TPR), *in situ* diffuse reflectance infrared Fourier

transform spectroscopy (DRIFTS), and oxygen storage capacity (OSC) measurements. The catalytic behaviour of supported-Rh solids towards phenol steam reforming was compared to a commercial Ni-based catalyst at the same experimental conditions.

2. Experimental

2.1. Catalyst development

Commercial Zr_{0.93}La_{0.07}O₂, Ce_{0.15}Zr_{0.85}O₂ and Ce_{0.13}Zr_{0.83}La_{0.04}O₂ (atom% composition) mixed metal oxides (MEL Chemicals, UK) were used as supports of Rh metal after calcination in air at 750 °C for 5 h. These metal oxides were synthesized by the same proprietary co-precipitation method. The supported-Rh catalysts were prepared in the laboratory by the wet impregnation method using Rh(NO₃)₃ (Aldrich) as a metal precursor. A given amount of precursor solution (distilled and de-ionised water was used as a solvent) corresponding to 0.5 wt% nominal Rh loading was used to impregnate at 60 °C and under continuous stirring each commercial mixed metal oxide. The solution pH was adjusted to 9.5 by drop-wise addition of ammonia solution until completion of impregnation. The thus obtained solid catalysts were dried overnight (~120 °C) and stored for further use.

2.2. Catalyst characterization

2.2.1. Catalyst texture and Rh dispersion measurements

The specific surface area (SSA, m² g⁻¹), pores volume (V_p, cm³ g⁻¹), and average pores diameter (d_p, nm) of the calcined (air, 750 °C/5 h) Zr_{0.93}La_{0.07}O₂, Ce_{0.15}Zr_{0.85}O₂ and Ce_{0.13}Zr_{0.83}La_{0.04}O₂ solids were determined by N₂ physical adsorption at 77 K using a Micromeritics Gemini III Surface Area and Pore size Analyser. Each measurement was taken after the samples were outgassed *in situ* at 200 °C under vacuum ($P \approx 1.3 \times 10^{-3}$) for 2 h. The dispersion of Rh metal was determined by H₂ selective chemisorption (H/Rh_s = 1/1) followed by TPD in He flow in a specially designed gas-flow system [33]. A 0.5-g catalyst sample and a 30 N mL min⁻¹ He flow rate were used. The fresh solid catalyst sample was first calcined in 20 vol%O₂/He gas mixture at 600 °C for 2 h and then reduced in pure H₂ (1 bar) at 200 °C for 2 h. After reduction, the catalyst was heated to 500 °C in He flow in order to desorb any H₂ that might have been spilled over the support. The catalyst was then cooled in He flow to 100 °C and the feed was switched to a 1 vol%H₂/He gas mixture for 30 min. Following this adsorption step, the catalyst was cooled in 1 vol%H₂/He to 30 °C and kept for 15 min. A switch to He flow was then made for 15 min and the temperature of the catalyst was increased to 700 °C in order to carry out a temperature-programmed desorption (TPD) experiment. Estimation of the mean Rh particle size was based on a spherical geometry [34]. It should be noted here that when the H₂ chemisorption step was conducted at 25 °C instead of 100 °C as previously mentioned, hydrogen desorption took place in the same temperature range as that observed following chemisorption at 100 °C. However, the amount of chemisorption (μmol H g_{cat}⁻¹) was about 20% lower in the case where the adsorption temperature was 25 °C. This result points out that on the present catalysts H₂ chemisorption was an activated process. It is also important to note here that the fact that HR-TEM studies revealed a mean Rh particle size similar to the one estimated from the H₂ chemisorption/TPD studies (Section 3.1.3), hydrogen spillover if occurred at 100 °C and under the chemisorption conditions used was negligible.

2.2.2. X-ray diffraction studies

The crystal structure of the calcined (air, 750 °C/5 h) Zr_{0.93}La_{0.07}O₂, Ce_{0.15}Zr_{0.85}O₂ and Ce_{0.13}Zr_{0.83}La_{0.04}O₂ solids

was checked by powder X-ray diffraction (XRD) using a Shimadzu 6000 diffractometer with $\text{CuK}\alpha$ radiation ($\lambda = 1.5418 \text{ \AA}$). About 100 mg of sample was crushed into a fine powder form and placed in a special glassy holder before XRD measurements. The diffractograms were recorded in the range of 2θ between 10° and 80° with a step scan of 2° min^{-1} . The primary mean crystallite size (d_c , nm) was determined using the Scherrer equation [35].

2.2.3. HR-TEM studies

High resolution transmission electron microscopy (HR-TEM) studies were performed on the $\text{Rh}/\text{Zr}_{0.93}\text{La}_{0.07}\text{O}_2$, $\text{Rh}/\text{Ce}_{0.15}\text{Zr}_{0.85}\text{O}_2$ and $\text{Rh}/\text{Ce}_{0.13}\text{Zr}_{0.83}\text{La}_{0.04}\text{O}_2$ catalysts (0.5 wt% Rh) in order to examine the size and morphology of Rh nanoparticles. All fresh catalysts were first calcined in 20 vol% O_2/He at 600°C for 2 h and then reduced in H_2 (1 bar) at 200°C before HR-TEM measurements. A 10-mg powder sample was dispersed in 5 mL of pure iso-octane and kept in an ultrasonic bath for 5 min. Droplets of the sample were then deposited onto a carbon-covered copper grid and left to dry at room T. A JEOL 2100F transmission electron microscope with a field emission gun (FEG) and a point resolution of 0.19 nm were used.

2.2.4. X-ray photoelectron spectroscopy studies

X-ray photoelectron spectroscopy (XPS) studies were conducted on a VG Escalab 200R electron spectrometer equipped with a hemispherical electron analyser and an $\text{MgK}\alpha$ ($h\nu = 1254.6 \text{ eV}$) X-ray source. The powder samples were pressed in an 8-mm diameter copper trough and fixed on the XYZ manipulator. The base pressure in the analysis chamber was maintained below 4×10^{-9} mbar during data acquisition. The pass energy of the analyser was set at 50 eV for which the resolution measured based on the full-width at half maximum (FWHM) of the $\text{Au } 4f_{7/2}$ core level was 1.7 eV. The binding energies were referenced to the C 1s peak at 284.9 eV (adventitious carbon). Data processing was performed with the provided XPS peak program, while XP spectra were deconvoluted with a least squared fitting routine after subtracting a Shirley background and using Gaussian/Lorentzian (90/10) product function. Surface atomic composition (atom%) was estimated using peak areas normalized on the basis of sensitivity factors [36]. The estimated error in the quantitative surface composition performed based on duplicate and/or triplicate measurements was less than 10%.

2.2.5. H_2 temperature-programmed reduction studies

H_2 temperature-programmed reduction (H_2 -TPR) experiments were conducted in a specially designed gas-flow system previously described [33] over the calcined commercial mixed metal oxides supports alone, and their respective supported-Rh catalysts. All solids were first calcined in 20 vol% O_2/He at 600°C for 2 h, purged in He flow for 15 min, and then quickly cooled to room T. A 2 vol% H_2/He gas mixture was then switched to the catalytic micro-reactor and the temperature was increased to 800°C ($\beta = 30^\circ\text{C min}^{-1}$). The chemical analysis of micro-reactor's gas effluent stream was performed with an *on line* quadrupole mass spectrometer (Omnistar, Balzers) equipped with a fast response inlet capillary/leak valve (SV1050, Balzers). The mass numbers (m/z) 2, 18, and 32 were used for H_2 , H_2O and O_2 monitoring, respectively. Based on a material balance, the rate of hydrogen consumption ($\mu\text{mol H}_2 \text{ g}^{-1} \text{ s}^{-1}$) versus temperature was estimated.

2.2.6. CO and CO_2 temperature-programmed desorption studies

CO and CO_2 temperature-programmed desorption (TPD) experiments were conducted in a specially designed gas-flow system described elsewhere [33]. The commercial mixed metal oxides (0.5 g) were first calcined *in situ* in 20 vol% O_2/He at 600°C for 2 h, whereas the supported-Rh catalysts (0.5 g) were activated in pure

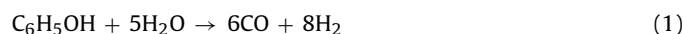
H_2 (1 bar) at 200°C for 2 h following calcination in 20 vol% O_2/He at 600°C for 2 h. Following these gas pre-treatment steps, the feed was changed to He for 15 min and the reactor was cooled to room temperature. The feed was subsequently switched to 3 vol% CO_2/He (CO_2 -TPD) or 2 vol% CO/He (CO -TPD) gas mixture for 30 min. A helium (He) flow (30 N mL min^{-1}) was then used until no signal of CO_2 and CO was detected in the mass spectrometer. The temperature of the solid was then increased to 700°C in He flow at the rate of $30^\circ\text{C min}^{-1}$. Calibration of the CO_2 ($m/z = 44$) and CO ($m/z = 28$) signals in the mass spectrometer was made based on standard 1 vol% CO_2/He and 1 vol% CO/He gas mixtures, respectively. For supported-Rh catalysts, following H_2 reduction, these were purged in He flow at 500°C , until no H_2 evolution was observed, and then cooled quickly to room temperature. The mass numbers (m/z) 2, 18, 28 and 44 were used for H_2 , H_2O , CO, and CO_2 monitoring, respectively in both CO- and CO_2 -TPDs.

2.2.7. Oxygen storage capacity (OSC) measurements

The Oxygen storage capacity, OSC ($\mu\text{mol O}_{\text{gcat}}^{-1}$) of $\text{Rh}/\text{Zr}_{0.93}\text{La}_{0.07}\text{O}_2$, $\text{Rh}/\text{Ce}_{0.15}\text{Zr}_{0.85}\text{O}_2$ and $\text{Rh}/\text{Ce}_{0.13}\text{Zr}_{0.83}\text{La}_{0.04}\text{O}_2$ solids (0.5 wt% Rh) was measured using the H_2/O_2 pulse injection technique [37,38]. The concentration ($\mu\text{mol O}_{\text{gcat}}^{-1}$) of reactive oxygen species present in the solid was estimated based on the amount of O_2 consumed during the re-oxidation step by successive oxygen pulses, the number of which is dependent on the size of the pulse and the kinetics of oxygen storage (surface/bulk diffusion) at the given temperature of treatment. The latter amount of oxygen is referred to as "Oxygen Storage Capacity Complete", OSCC. The amount of the most reactive oxygen (labile oxygen) of the catalyst is defined as the amount of oxygen that reacted during the first H_2 pulse (50 μmol), or equivalently the amount of oxygen consumed during the re-oxidation step, and this is named "Oxygen Storage Capacity", OSC. The catalyst used (50 mg, powder form) was first pre-treated in 20 vol% O_2/He at a given temperature, T_{OSC} (350 – 550°C) for 1 h, flushed in He flow for 15 min at T_{OSC} , followed by H_2/O_2 pulse(s).

2.3. Catalytic activity studies

Steady-state catalytic measurements for the steam reforming of phenol in the 350 – 550°C range were carried out in a Micro-reactivity Pro apparatus (CSIC, Madrid-Spain) previously described [31]. A 0.3-g of supported-Rh catalyst was loaded in a fixed bed quartz micro-reactor. The total flow rate used was $200 \text{ N mL min}^{-1}$ ($\text{GHSV} \sim 54,000 \text{ h}^{-1}$), and the reaction feed composition consisted of 0.6% $\text{C}_6\text{H}_5\text{OH}/40\% \text{H}_2\text{O}/59.4\% \text{He}$, simulating the phenol and water concentrations encounter at the inlet (bottom) of a fluidized bed reactor used in steam gasification of wood-biomass [12]. Initially, the catalyst sample was pre-treated *in situ* in 20 vol% O_2/He at 600°C for 2 h and then reduced in pure H_2 (1 bar) at 200°C for 2 h. All catalytic tests were conducted at 1 bar total pressure. Following reaction at a given temperature, the catalyst was pre-treated in 20 vol% O_2/He at 600°C for 2 h and then reduced in H_2 flow (1 bar) at 200°C for 2 h before proceeding to the next reaction temperature. The steam reforming of phenol can be described by the following reaction network [29,30,31,32,39,40]:



The conversion of phenol (X_p , %) was estimated based on the following relationship:

$$X_p(\%) = \frac{(F_{\text{CO}}^{\text{exp}} + F_{\text{CO}_2}^{\text{exp}})}{6F_p^{\text{in}}} \times 100 \quad (3)$$

where $F_{\text{CO}}^{\text{exp}}$ and $F_{\text{CO}_2}^{\text{exp}}$ is the molar flow rate (mol s^{-1}) of CO and CO_2 , respectively, at the exit of the micro-reactor, and F_{P}^{in} is the feed molar flow rate (mol s^{-1}) of phenol. It is important to note that only very small concentrations of benzene and methane were experimentally measured in the product gas stream at the exit of the micro-reactor (wet-basis), and these are not included in Eq. (3). The hydrogen yield, y_{H_2} (%) was estimated based on the following relationship:

$$Y_{\text{H}_2}(\%) = \frac{y_{\text{H}_2}^{\text{out}}}{y_{\text{H}_2}^{\text{max}}} \times 100 \quad (4)$$

where $y_{\text{H}_2}^{\text{out}}$ is the composition (mol%, dry-basis) of hydrogen at the exit gas stream of the micro-reactor, and $y_{\text{H}_2}^{\text{max}}$ is the composition (mol%, dry-basis) of hydrogen expected when complete conversion of phenol (reaction 1) and CO (reaction 2) is achieved. For the present feed composition (0.6% $\text{C}_6\text{H}_5\text{OH}$ /40% H_2O /59.4% He), $y_{\text{H}_2}^{\text{max}}$ is 11.76 mol% (dry-basis).

2.4. In situ DRIFTS studies

2.4.1. CO_2 and H_2O chemisorption

A Perkin-Elmer Spectrum GX II FTIR spectrometer equipped with a high-temperature/high pressure controllable DRIFTS cell (Harrick, Praying Mantis) was used to perform *in situ* DRIFTS CO_2 and H_2O chemisorption studies over the $\text{Rh/Ce}_{0.15}\text{Zr}_{0.85}\text{O}_2$ and $\text{Rh/Ce}_{0.13}\text{Zr}_{0.83}\text{La}_{0.04}\text{O}_2$ solids. The catalyst sample (~ 35 mg) in a very fine powder form was placed firmly into the ceramic cup of the DRIFTS cell. Chemisorption was conducted using a 3 vol% CO_2/He (50 N mL min^{-1}) and 40 vol% $\text{H}_2\text{O}/\text{He}$ ($100 \text{ N mL min}^{-1}$) gas mixtures at 450°C for 30 min. Each sample was first pre-treated *in situ* in 20 vol% O_2/Ar at 600°C for 2 h. In the case of CO_2 chemisorption, the samples were first reduced *in situ* in pure H_2 (1 bar) at 200°C for 2 h following pre-treatment in 20 vol% O_2/Ar at 600°C for 2 h. Signal averaging was set to 50 scans per spectrum at a 2 cm^{-1} spectral resolution in the $4000\text{--}400 \text{ cm}^{-1}$ range. The DRIFTS spectra presented here correspond only to the spectra of the adsorbed phase; the spectrum of the solid itself taken in Ar flow at the desired temperature was subtracted. DRIFTS spectra when necessary were smoothed to remove high frequency noise and further analyzed using the software Spectrum for Windows. Deconvolution and curve fitting procedures were performed according to reported guidelines [41] and using Gaussian peak line shape [42].

2.4.2. Operando WGS reaction studies

Operando studies were performed in a specially designed gas-flow system using combined DRIFTS (reaction cell) and mass spectroscopy for gas product analysis [43,44]. The WGS reaction was studied at 450°C over the $\text{Rh/Ce}_{0.15}\text{Zr}_{0.85}\text{O}_2$ and $\text{Rh/Ce}_{0.13}\text{Zr}_{0.83}\text{La}_{0.04}\text{O}_2$ solids. The reaction feed used was 1 vol% $\text{CO}/40 \text{ vol}\% \text{H}_2\text{O}/59 \text{ vol}\% \text{He}$, the latter simulating the composition measured at the exit of the micro-reactor under phenol steam reforming reaction conditions (see Section 2.3) at a total flow rate of $100 \text{ N mL min}^{-1}$. The effect of H_2 in the feed stream on the rate of WGS reaction was also investigated using the feed composition 1 vol% $\text{CO}/40 \text{ vol}\% \text{H}_2\text{O}/7 \text{ vol}\% \text{H}_2/52 \text{ vol}\% \text{He}$. The spectrum of the solid recorded in 40 vol% $\text{H}_2\text{O}/\text{Ar}$ flow ($100 \text{ N mL min}^{-1}$), following calcination in 20 vol% O_2/Ar at 600°C for 2 h and reduction in H_2 at 200°C for 2 h, was subtracted from the spectrum of the solid recorded under WGS reaction conditions. The effluent stream from the DRIFTS cell was directed to the mass spectrometer (Balzer, Omnistar, 1–300 amu) for recording the evolution of H_2 , CO_2 and CO gas products. Based on a material balance, the rates of H_2 and CO_2 production ($\mu\text{mol g}^{-1} \text{ s}^{-1}$) were estimated. The DRIFTS cell was

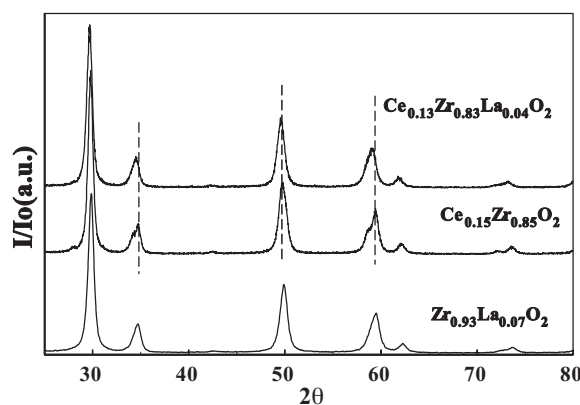


Fig. 1. Powder X-ray diffraction patterns of $\text{Zr}_{0.93}\text{La}_{0.07}\text{O}_2$, $\text{Ce}_{0.15}\text{Zr}_{0.85}\text{O}_2$ and $\text{Ce}_{0.13}\text{Zr}_{0.83}\text{La}_{0.04}\text{O}_2$ solids after calcination in air at 750°C for 5 h.

operated under differential conditions, thus intrinsic kinetic rates could be estimated.

3. Results and discussion

3.1. Catalyst characterization studies

3.1.1. Catalyst texture

The specific surface area (SSA), pores volume (V_p), and mean pores diameter (d_p) of the $\text{Zr}_{0.93}\text{La}_{0.07}\text{O}_2$, $\text{Ce}_{0.15}\text{Zr}_{0.85}\text{O}_2$ and $\text{Ce}_{0.13}\text{Zr}_{0.83}\text{La}_{0.04}\text{O}_2$ solids investigated are given in Table 1. It is observed that both La^{3+} -containing mixed metal oxides exhibit higher SSA, pores volume and mean pores diameter values compared to $\text{Ce}_{0.15}\text{Zr}_{0.85}\text{O}_2$ solid. The presence of mesoporosity is evidenced for all three materials with a mean pores diameter in the 8.2–9.2 nm range. The V_p was found to increase from 0.12 to $0.19 \text{ cm}^3 \text{ g}^{-1}$ (58% increase), and the SSA from 42.6 to $65.3 \text{ m}^2 \text{ g}^{-1}$ (35% increase, Table 1) after introducing 4 atom% La^{3+} in the Ce–Zr–O matrix. On the other hand, a slight decrease in the mean primary crystal size (d_c) is obtained (Table 1). Similar results were reported by Vidmar et al. [45] in their study of the effect of trivalent dopant (Y^{3+} , La^{3+} and Ga^{3+}) on the redox properties of Ce–Zr–O solid solution. In particular, it was reported that at dopant contents equal to or higher than 2.5 mol% the SSA was increased. Additionally, Yue et al. [46] reported that addition of 1 wt% of rare earth metal (La, Pr, Nd, Sm, Y) into the Ce–Zr–O/ Al_2O_3 solid stabilizes its surface area to higher values, and improves also the tolerance of alumina against sintering. All these observations clearly suggest that the textural properties of the present mixed metal oxide supports are related to their particular bulk chemical composition.

3.1.2. XRD studies

Powder X-ray diffraction patterns of $\text{Zr}_{0.93}\text{La}_{0.07}\text{O}_2$, $\text{Ce}_{0.15}\text{Zr}_{0.85}\text{O}_2$ and $\text{Ce}_{0.13}\text{Zr}_{0.83}\text{La}_{0.04}\text{O}_2$ solids were recorded after calcination in air at 750°C for 5 h. As shown in Fig. 1, $\text{Zr}_{0.93}\text{La}_{0.07}\text{O}_2$ revealed a single crystalline phase corresponding to the tetragonal structure of ZrO_2 due to the formation of La–Zr–O solid solution. It is well known that the chemical and physical properties of ZrO_2 can be modified by adding cations of lower valence, such as Y^{3+} , La^{3+} , Mg^{2+} and Ca^{2+} [47]. These dopants stabilize the cubic or tetragonal phase of ZrO_2 at room temperature forming a solid solution in which the replacement of Zr^{4+} with cations of lower valence induces generation of oxygen vacancies within the ZrO_2 lattice [47,48,49]. The formation of a single “homogeneous” pseudo-tetragonal CeO_2 – ZrO_2 solid solution might be noticed for the $\text{Ce}_{0.15}\text{Zr}_{0.85}\text{O}_2$ and $\text{Ce}_{0.13}\text{Zr}_{0.83}\text{La}_{0.04}\text{O}_2$ solids (Fig. 1). However, it is appropriate to state here that due

Table 1

Textural and mean primary crystal size characteristics of commercial $\text{Zr}_{0.93}\text{La}_{0.07}\text{O}_2$, $\text{Ce}_{0.15}\text{Zr}_{0.85}\text{O}_2$ and $\text{Ce}_{0.13}\text{Zr}_{0.83}\text{La}_{0.04}\text{O}_2$ mixed metal oxides after calcination in air at 750 °C for 5 h and *in situ* out gassing at 200 °C under vacuum for 2 h.

Support composition	SSA ($\text{m}^2 \text{g}^{-1}$)	Pores volume V_p ($\text{cm}^3 \text{g}^{-1}$)	Mean pores diameter, d_p (nm)	Mean primary crystal size, d_c (nm)
$\text{Zr}_{0.93}\text{La}_{0.07}\text{O}_2$	68.8	0.21	9.2	11.8
$\text{Ce}_{0.15}\text{Zr}_{0.85}\text{O}_2$	42.6	0.12	8.2	12.5
$\text{Ce}_{0.13}\text{Zr}_{0.83}\text{La}_{0.04}\text{O}_2$	65.3	0.19	9.0	11.8

to the complexity of the phase diagram related to $\text{Ce}_x\text{Zr}_{1-x}\text{O}_2$, the phase homogeneity of these solids is doubtful to be verified by XRD and Raman techniques [50]. More complex techniques such as neutron diffraction and Eu(III) luminescence spectroscopy proved to be able to identify inhomogeneities for samples that appear “homogeneous” from XRD analyses, revealing the presence of nano-domains with different compositions [50].

The small spitting near 30° and 60° 2θ for $\text{Ce}_{0.15}\text{Zr}_{0.85}\text{O}_2$ (Fig. 1) is an evidence for a cubic phase ceria. In the case of $\text{Ce}_{0.13}\text{Zr}_{0.83}\text{La}_{0.04}\text{O}_2$, no extra characteristic diffraction peaks corresponding to single phase La_2O_3 were detected. It is important to note that diffraction peaks corresponding to $\text{Ce}_{0.15}\text{Zr}_{0.85}\text{O}_2$ were slightly shifted to smaller 2θ Bragg angles with the addition of 4 atom% La (see perpendicular broken lines). The latter result indicates that substitution of Ce^{4+} and Zr^{4+} for La^{3+} cations increased the interplanar distance in the Ce–Zr–O lattice, fact that is related to the larger ionic radii of La^{3+} (1.18 Å) compared to Zr^{4+} (0.84 Å) and Ce^{4+} (0.97 Å). The formation of a cubic structure even for high Zr^{4+} contents by the addition of trivalent cations, M^{3+} ($\text{M} = \text{La}^{3+}$, Y^{3+} , Ga^{3+}) in Ce–Zr–O was also reported [51,52].

The mean primary crystal size of the calcined $\text{Zr}_{0.93}\text{La}_{0.07}\text{O}_2$, $\text{Ce}_{0.15}\text{Zr}_{0.85}\text{O}_2$ and $\text{Ce}_{0.13}\text{Zr}_{0.83}\text{La}_{0.04}\text{O}_2$ solids is reported in Table 1, and is in the 11.8–12.5 nm range, leading to the conclusion that these solids retain a nano-crystalline nature with expected increased thermal stability and tolerance against sintering [46,47]. It is noted that both La^{3+} -doped mixed metal oxides led to the same mean primary crystal size.

3.1.3. Rhodium dispersion and particle size

The dispersion (D , %) of Rh metal (see Section 2.2.1) was found to be 25%, 33%, and 54%, and the corresponding mean Rh particle size 4.0, 3.0 and 1.9 nm for the 0.5%Rh/ $\text{Ce}_{0.15}\text{Zr}_{0.85}\text{O}_2$, 0.5%Rh/ $\text{Zr}_{0.93}\text{La}_{0.07}\text{O}_2$, and 0.5%Rh/ $\text{Ce}_{0.13}\text{Zr}_{0.83}\text{La}_{0.04}\text{O}_2$ catalysts, respectively. It is observed that the addition of La^{3+} in the $\text{Ce}_{0.15}\text{Zr}_{0.85}\text{O}_2$ matrix led to an increase of Rh dispersion and to a smaller mean Rh particle size, thus a higher concentration of surface metal active sites ($\mu\text{mol Rh}_s \text{g}^{-1}$). In particular, Rh dispersion was nearly doubled with the introduction of 4 atom% La^{3+} in the $\text{Ce}_{0.15}\text{Zr}_{0.85}\text{O}_2$ solid solution. It is suggested that the different electron density around the oxygen atoms in each of the three mixed metal oxide support compositions influences the strength of Rh–O–M (M') bond (M , M' : different metal cations in the mixed metal oxide supports) established after Rh deposition followed by calcination and reduction pre-treatments [29]. Thus, there is a dependence of the binding energy of Rh on support chemical composition. An enhancement of Rh metal dispersion by the addition of La^{3+} onto the Al_2O_3 support was also reported [53,54].

HR-TEM studies conducted over the supported-Rh catalysts confirmed the correctness of the H_2 chemisorption procedure applied, based on which the metal dispersion and Rh particle size were estimated. Fig. 2a–c show HR-TEM images obtained on the Rh/ $\text{Zr}_{0.93}\text{La}_{0.07}\text{O}_2$, Rh/ $\text{Ce}_{0.15}\text{Zr}_{0.85}\text{O}_2$ and Rh/ $\text{Ce}_{0.13}\text{Zr}_{0.83}\text{La}_{0.04}\text{O}_2$ solids, respectively, after calcination in 20 vol% O_2 /He at 600 °C for 2 h followed by reduction in H_2 (1 bar) at 200 °C for 2 h. The excellent quality of micrographs recorded allowed the estimation of the

Rh mean particle size. This was found to be 2.6 (± 1.0), 3.5 (± 1.4) and 2.1 (± 0.8) nm for the Rh/ $\text{Zr}_{0.93}\text{La}_{0.07}\text{O}_2$, Rh/ $\text{Ce}_{0.15}\text{Zr}_{0.85}\text{O}_2$ and Rh/ $\text{Ce}_{0.13}\text{Zr}_{0.83}\text{La}_{0.04}\text{O}_2$ catalysts, respectively. The Rh particle size distributions were obtained after counting about 200 particles, which resulted in the above mentioned mean Rh particle size and standard deviation. It is noted that an approximate spherical geometry for Rh particles is observed (Fig. 2), making the relevant assumption for Rh dispersion estimation valid (Section 2.2.1).

3.1.4. XPS studies

The chemical state of the elements and their relative abundance on the surface region of the catalysts was investigated by X-ray photoelectron spectroscopy. Fig. 3a presents X-ray photoelectron spectra for the Rh 3d energy level after the Rh/ $\text{Ce}_{0.13}\text{Zr}_{0.83}\text{La}_{0.04}\text{O}_2$ catalyst was calcined in 20 vol% O_2 /He at 600 °C for 2 h (upper spectrum) and then reduced in pure H_2 at 200 °C for 2 h (lower spectrum) in the pre-treatment chamber (1 bar) of the XPS instrument. As shown in the upper spectrum of Fig. 3a, the most intense Rh 3d_{5/2} peak of the Rh 3d doublet occurs at 308.9 eV. This binding energy (BE) indicates clearly that rhodium is in the Rh^{3+} oxidation state, either as small Rh_2O_3 nanoparticles or Rh–O–Ce(Zr) linkages [55,56]. These peaks were shifted to lower BE's: 307.1 (Rh 3d_{5/2}) and 311.7 eV (Rh 3d_{3/2}) following H_2 reduction (lower spectrum), and they are unambiguously attributed to Rh^0 [55,56]. As the full width at half maximum (FWHM) of the Rh 3d_{5/2} peak is relatively low, only one kind of Rh species is present in the reduced catalyst, which means that complete reduction of Rh_2O_3 was accomplished at the applied pre-treatment conditions. Similar XP spectra were recorded for the Rh/ $\text{Zr}_{0.93}\text{La}_{0.07}\text{O}_2$ and Rh/ $\text{Ce}_{0.15}\text{Zr}_{0.85}\text{O}_2$ solids. As the Rh crystallite size determined from HR-TEM images of the H_2 reduced catalysts is in the 2.1–3.5 nm range (several hundred Rh atoms in the crystal), this is somewhat smaller than the Rh3d_{5/2} electron mean free path, indicating that the BE value measured includes all Rh atoms. Thus, it is expected that Rh-support interactions are substantially weakened in the reduced state of the catalyst compared to the oxidized one.

Table 2 reports the binding energies of the Rh 3d_{5/2}, Zr 3d_{5/2} and O 1s XP peaks measured in the reduced Rh/ $\text{Zr}_{0.93}\text{La}_{0.07}\text{O}_2$, Rh/ $\text{Ce}_{0.15}\text{Zr}_{0.85}\text{O}_2$ and Rh/ $\text{Ce}_{0.13}\text{Zr}_{0.83}\text{La}_{0.04}\text{O}_2$ solids. The binding energy values that correspond to Ce 3d_{5/2} and La 3d_{5/2} were found to be 882.9 and 834.7 eV in both respective solids. The BE values for Ce 3d_{5/2}, Zr 3d_{5/2} and La 3d_{5/2} are coherent with the values expected for their respective metal oxides [57,58,59,60,61,62].

Table 2

Characteristic binding energies (eV) of core electrons of reduced^a supported-Rh catalysts.

Catalyst	Rh 3d _{5/2}	Zr 3d _{5/2}	O 1s
0.5 wt%Rh/ $\text{Zr}_{0.93}\text{La}_{0.07}\text{O}_2$	307.1	182.2	529.9 (69) 531.6 (31)
0.5 wt%Rh/ $\text{Ce}_{0.15}\text{Zr}_{0.85}\text{O}_2$	307.1	182.2	530.0 (74) 531.7 (26)
0.5 wt%Rh/ $\text{Ce}_{0.13}\text{Zr}_{0.83}\text{La}_{0.04}\text{O}_2$	307.1	182.1	529.9 (78) 531.6 (22)

^a Reduction conditions: H_2 (1 bar) at 200 °C for 2 h following calcination in 20 vol% O_2 /He at 600 °C for 2 h.

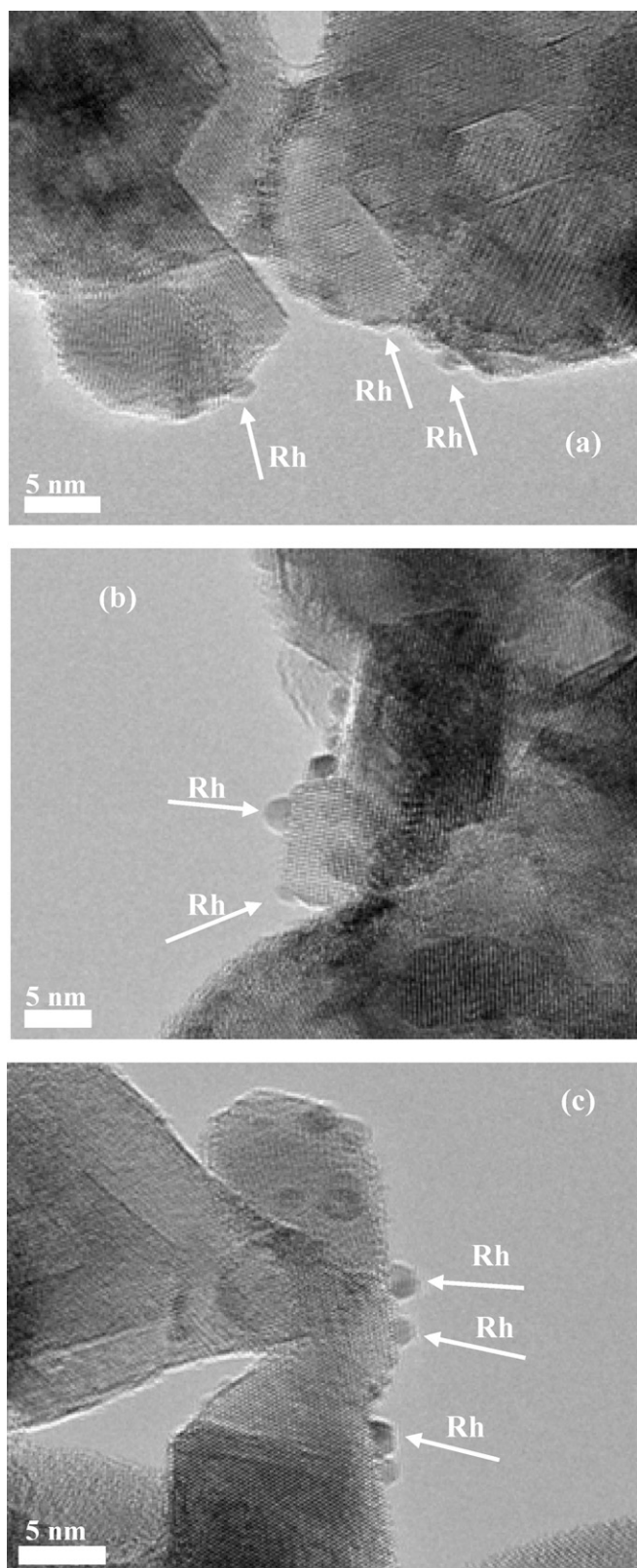


Fig. 2. HR-TEM images of (a) 0.5 wt% Rh/Zr_{0.93}La_{0.07}O₂, (b) 0.5 wt% Rh/Ce_{0.15}Zr_{0.85}O₂ and (c) 0.5 wt% Rh/Ce_{0.13}Zr_{0.83}La_{0.04}O₂ solids.

Rhodium appears to be fully reduced (Rh⁰) in all catalysts samples as previously mentioned. However, a small concentration of Rh located at the metal-support interface, which is bound with the support oxygen anions, is expected to be found in an oxidized

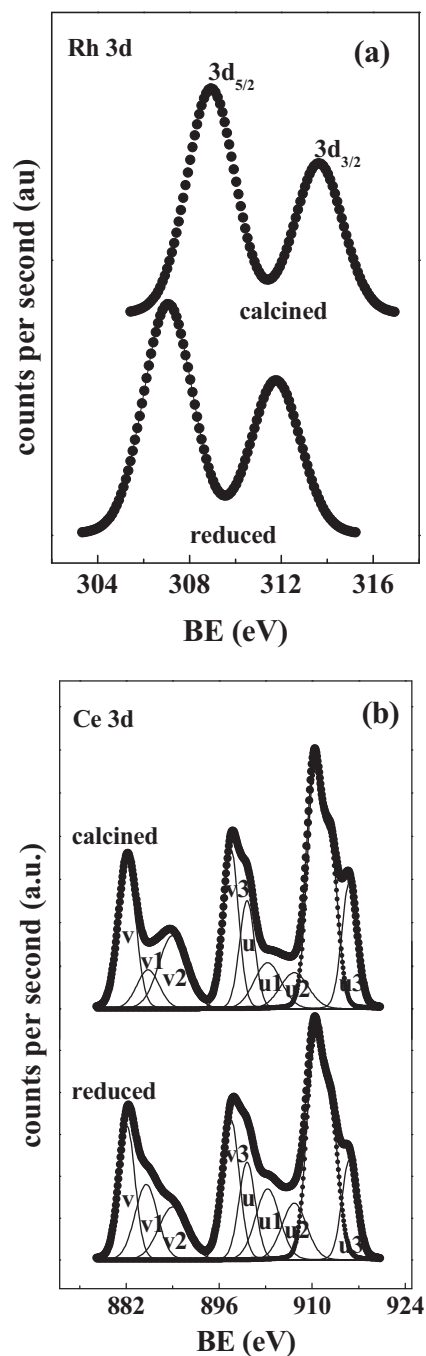


Fig. 3. X-ray photoelectron spectra of (a) Rh 3d and (b) Ce 3d following calcination (20 vol%O₂/He, 600 °C, 2 h) (upper spectrum), and reduction (H₂, 200 °C, 2 h) (lower spectrum) obtained on the 0.5 wt% Rh/Ce_{0.13}Zr_{0.83}La_{0.04}O₂ solid.

state, and this is not possible to be quantified by the XPS. In the case of O 1s core electrons, two peaks with BE at 529.9/530 and 531.6/531.7 eV are reported in Table 2. These BE values are characteristic of lattice oxygen and adsorbed surface oxygen-containing species, respectively [63]. The latter species may be due to carbonates derived from atmospheric CO₂ and/or to hydroxyl groups formed by water molecules, persisting after calcination and reduction treatments. The values reported in parentheses for the O 1s peak refer to the percentage of the two types of oxygen, lattice or adsorbed for the H₂-reduced Rh catalysts. From these values it is seen that Rh/Ce_{0.13}Zr_{0.83}La_{0.04}O₂ exposes a higher concentration of surface lattice oxygen compared to Rh/Ce_{0.15}Zr_{0.85}O₂ and

Rh/Zr_{0.93}La_{0.07}O₂, in full agreement with the OSC measurements (Section 3.1.8). The opposite behaviour is found for the adsorbed surface oxygen-containing species.

Table 3 reports the surface atom% composition of supported-Rh catalysts following hydrogen reduction. It is observed that Rh/Ce_{0.13}Zr_{0.83}La_{0.04}O₂ exhibits the highest surface concentration of rhodium and oxygen, where Rh exposure is significantly enhanced with the addition of La³⁺ into the Ce_{0.15}Zr_{0.85}O₂ support (Rh/Ce_{0.13}Zr_{0.83}La_{0.04}O₂). The latter is in harmony with the higher Rh dispersion determined for the Rh/Ce_{0.13}Zr_{0.83}La_{0.04}O₂ compared to Rh/Ce_{0.15}Zr_{0.85}O₂ solid (Section 3.1.3). The small concentration of carbonates detected for all supported-Rh catalysts is due to the exposure of the samples in the air during handling and transfer to the XPS instrument, not removed under the *in situ* calcination at 600 °C followed by H₂ reduction at 200 °C performed in the pre-treatment chamber of the XPS instrument.

Fig. 3b shows Ce 3d XP spectra obtained after calcination and reduction of the Rh/Ce_{0.13}Zr_{0.83}La_{0.04}O₂ solid as previously mentioned. It is observed that there are two sets of spin-orbit multiplets, which are labeled as v and u, corresponding to the Ce 3d_{5/2} and Ce 3d_{3/2} ionization levels, respectively. This result indicates the presence of Ce⁴⁺ and Ce³⁺ in the ceria matrix [57,58,59,60]. More precisely, the peaks assigned to Ce⁴⁺ for the Ce 3d_{5/2} level are: v (882.9 eV), v2 (889.1 eV) and v3 (897.9 eV), while the corresponding peaks for the Ce 3d_{3/2} energy level are: u (900.3 eV), u2 (907.2 eV) and u3 (915.8 eV). For the Ce³⁺ species, the components are: v1 (885.6 eV) and u1 (903.4 eV). The v and v2 features, and the u and u2 features are shake-down signals due to charge transfer from the ligand (O 2p) to the metal (Ce 4f). These doublets are assigned to the strong mixing of 3d⁹4f² and 3d⁹f¹ Ce (IV) final electronic states [57,58,59,60,61]. The peaks labeled v3 and u3 are usually assigned to the 3d⁹4f⁰ Ce (IV) photoemission final electronic state, while states v1 and u1 belong to unique photoelectron features arising from the Ce³⁺ electronic state [57]. Similar 3d XPS electronic structures have been also reported for other CeO₂–ZrO₂ solid solutions [59,60,61]. The overlapping Zr MNN Auger peaks near 910 eV [61] are also shown in Fig. 3b.

By comparing the Ce 3d XP spectra recorded following reduction and oxidation of the Rh/Ce_{0.13}Zr_{0.83}La_{0.04}O₂ catalyst, it can be observed that the peak areas approximately at 885.6 eV (v1) and 903.4 eV (u1) increased upon H₂ reduction when compared after calcination treatment. The latter indicates that fraction of surface Ce⁴⁺ present in the solid is reduced to Ce³⁺. These results fit well with what has been reported [58], in that practically the progressive reduction of Ce⁴⁺ into Ce³⁺ results in a decrease of the electronic configuration 4f⁰ (v3 and u3), and an increase in v1 and u1 at the expense of v2 and u2. A surface atom ratio of Ce⁴⁺/Ce³⁺ = 13.3 was estimated in the case of the calcined solid, whereas this ratio was found to be 2.1 after hydrogen reduction at 200 °C, indicating significant reduction of Ce⁴⁺ into Ce³⁺, in harmony with the H₂-TPR studies to be presented next. The relative percentage of Ce⁴⁺ and Ce³⁺ species was estimated by using the intensity of the Ce 3d_{5/2} components relative to Ce⁴⁺ (v, v2, v3) and Ce³⁺ (v1) ones according to the literature [64].

3.1.5. H₂-TPR studies

Fig. 4a and b present H₂-TPR traces obtained on the three mixed metal oxide supports alone and their corresponding supported-Rh catalysts, respectively. Reduction of Ce_{0.15}Zr_{0.85}O₂ and Ce_{0.13}Zr_{0.83}La_{0.04}O₂ solids starts at about 300 °C with broad reduction peaks in the 500–800 °C range, while reduction of Zr_{0.93}La_{0.07}O₂ is obtained only in the 600–800 °C range. This illustrates that the M–O–M and M–O–M' (M, M' different metal cations) bonds strength associated with surface and sub-surface oxygen species is higher in Zr_{0.93}La_{0.07}O₂ than in the other solids. The

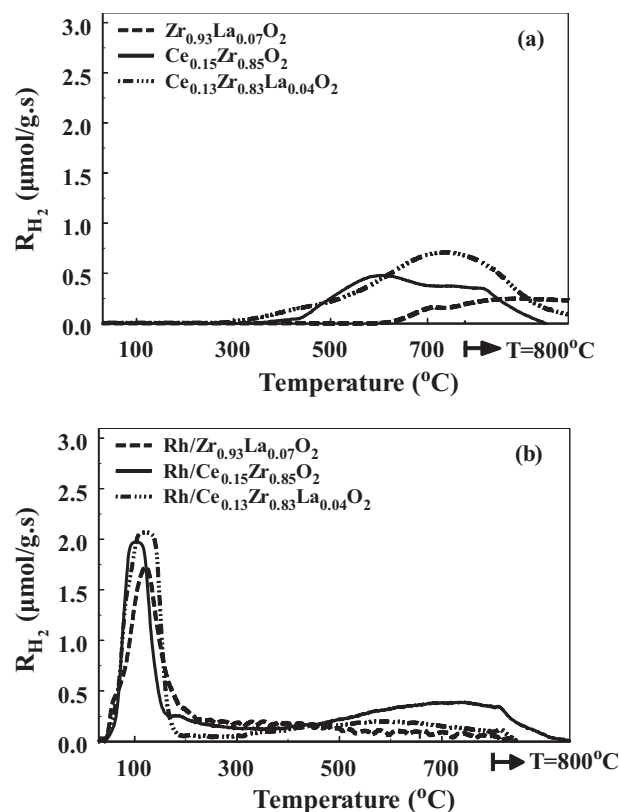


Fig. 4. H₂-TPR traces in terms of rate of hydrogen consumption ($\mu\text{mol H}_2 \text{ g}^{-1} \text{ s}^{-1}$) versus temperature obtained on (a) Zr_{0.93}La_{0.07}O₂, Ce_{0.15}Zr_{0.85}O₂ and Ce_{0.13}Zr_{0.83}La_{0.04}O₂ solids, and (b) 0.5 wt% Rh/Zr_{0.93}La_{0.07}O₂, 0.5 wt% Rh/Ce_{0.15}Zr_{0.85}O₂, and 0.5 wt% Rh/Ce_{0.13}Zr_{0.83}La_{0.04}O₂ solids. $F_{\text{H}_2/\text{He}} = 30 \text{ N mL min}^{-1}$; $\beta = 30^\circ \text{C min}^{-1}$; $W_{(a)} = 0.5 \text{ g}$; $W_{(b)} = 0.2 \text{ g}$.

H₂-TPR trace of Zr_{0.93}La_{0.07}O₂ consists of two weak broad peaks centered at 717 and 800 °C (isothermal reduction). It was reported [47,65,66] that ZrO₂ can be reduced only to a small extent above 500 °C. On the other hand, La₂O₃ cannot be easily reduced below 1000 °C [67], whereas a H₂-TPR peak centered at 810 °C was interpreted as due to the reduction of La₂O₂CO₃ into La₂O₃, CO₂ and H₂O [68]. It is suggested that H₂ reduction peaks for Zr_{0.93}La_{0.07}O₂ are due to reduction of Zr⁴⁺ in Zr–O–Zr and to a lesser extent in Zr–O–La–O lattice positions. The Ce_{0.15}Zr_{0.85}O₂ solid solution exhibits a strong and broad reduction peak at 610 °C with a large and broad tail on its falling part. In the case of Ce_{0.13}Zr_{0.83}La_{0.04}O₂, a single broad reduction peak centered at 742 °C was observed with a shoulder on its rising part. By comparing the H₂-TPR traces of Ce_{0.15}Zr_{0.85}O₂ and Ce_{0.13}Zr_{0.83}La_{0.04}O₂ solids it is observed that the presence of La³⁺ results in a shift of reduction temperatures towards higher values in agreement with the work of Vidmar et al. [45].

The area under the H₂-TPR traces is directly proportional to the amount of lattice oxygen reacted off by hydrogen. This amount was found to be: Ce_{0.13}Zr_{0.83}La_{0.04}O₂ ($366 \mu\text{mol g}^{-1}$) > Ce_{0.15}Zr_{0.85}O₂ ($263 \mu\text{mol g}^{-1}$) > Zr_{0.93}La_{0.07}O₂ ($52 \mu\text{mol g}^{-1}$). It is clearly observed that the presence of La³⁺ in an amount of 4 atom% results in an increase in the reducibility of Ce–Zr–La–O compared to Ce–Zr–O solid solution. A similar observation was also reported by Guo et al. [69] for the Ce_{0.50}Zr_{0.50}O₂ and Ce_{0.35}Zr_{0.55}La_{0.10}O_{1.95} solid solutions.

Fig. 4b presents H₂-TPR traces of the supported-Rh catalysts. It is clearly seen that part of the reduction trace observed in the bare supports (Fig. 4a) was shifted to lower reduction temperatures, e.g., 200–300 °C (Fig. 4b). After hydrogen reduction of Rh₂O₃ to Rh_x⁰ at temperatures lower than 200 °C, atomic hydrogen species formed

Table 3
Surface composition (atom%) of the supported-Rh catalysts following reduction^a.

Catalyst composition	Rh	La	Zr	Ce	O	Carbonates
Rh/Zr _{0.93} La _{0.07} O ₂	0.2	4.0	25.5	–	69.5	0.8
Rh/Ce _{0.15} Zr _{0.85} O ₂	0.2	–	25.9	5.9	66.8	1.2
Rh/Ce _{0.13} Zr _{0.83} La _{0.04} O ₂	0.4	2.5	16.2	5.8	74.2	0.9

^a Reduction conditions: H₂ (1 bar) at 200 °C for 2 h following calcination in 20 vol%O₂/He at 600 °C for 2 h.

by H₂ chemisorption on Rh_x⁰ can spill over from the metal to the support, thus favouring its reduction to occur at lower temperatures, e.g., 200–300 °C (Fig. 4b) [53,70], result that is supported by XPS studies (Section 3.1.4). As shown in Fig. 4b, all supported-Rh catalysts exhibit a large well-defined sharp peak in the 50–175 °C range due to the reduction of Rh₂O₃. Specifically, peaks with maxima at 126, 106 and 123 °C have appeared for the Rh/Zr_{0.93}La_{0.07}O₂, Rh/Ce_{0.15}Zr_{0.85}O₂ and Rh/Ce_{0.13}Zr_{0.83}La_{0.04}O₂ catalysts, respectively, in excellent agreement with the work of Rao et al. [71] and Fornasiero et al. [72]. It is worth mentioning that Rh₂O₃ reduction temperatures in the fully oxidized Rh/Ce_{0.13}Zr_{0.83}La_{0.04}O₂ are slightly higher than in Rh/Ce_{0.15}Zr_{0.85}O₂. This indicates that Rh and Ce_{0.13}Zr_{0.83}La_{0.04}O₂ exhibit stronger metal-support interactions. It was reported [73] that higher temperatures are required for the reduction of Rhⁿ⁺ after the addition of La³⁺ onto a SiO₂ support.

The total amount of H₂ consumed in the 25–800 °C range for the Rh/Zr_{0.93}La_{0.07}O₂, Rh/Ce_{0.13}Zr_{0.83}La_{0.04}O₂ and Rh/Ce_{0.15}Zr_{0.85}O₂ solids was found to be 373, 481, and 634 μmol_{gcat}^{−1}, respectively. A larger amount of H₂ was estimated to be consumed in the 30–250 °C range in the case of Rh/Ce_{0.13}Zr_{0.83}La_{0.04}O₂ compared to Rh/Ce_{0.15}Zr_{0.85}O₂ after considering that all the Rh (0.5 wt%) initially present as Rh₂O₃ (before the start of H₂-TPR) is reduced to Rh_x⁰ (30–250 °C) in all supported Rh catalyst samples. The latter implies that the presence of La³⁺ enhances surface reduction in the Ce–Zr–La–O support at low temperatures.

3.1.6. CO₂ chemisorption followed by TPD studies

Fig. 5a presents CO₂-TPD profiles obtained on the pre-calcined Zr_{0.93}La_{0.07}O₂, Ce_{0.15}Zr_{0.85}O₂ and Ce_{0.13}Zr_{0.83}La_{0.04}O₂ solid supports following chemisorption of CO₂ at 30 °C. Three different kinds of basic sites in terms of strength can be distinguished, namely: weak, moderate and strong, according to the peak maximum desorption temperatures of CO₂ obtained [74,75,76,77,78,79,80]. In the case of Zr_{0.93}La_{0.07}O₂, all three kinds of basic sites were observed. In particular, four distinct CO₂ desorption peaks with peak maxima at 86, 155, 205 and 238 °C accompanied by a large and broad shoulder at the falling part of the high-temperature peak were observed. These CO₂-TPD peaks could be assigned to one weak, two moderate and one strong basic site, respectively [74]. Three well resolved and intense CO₂ peaks centered at 89, 190 and 247 °C were detected in Ce_{0.13}Zr_{0.83}La_{0.04}O₂, while a single distinct peak with maximum at 92 °C, which corresponds to a weak basic site, with a tail at the falling part of it was detected in the case of Ce_{0.15}Zr_{0.85}O₂, in agreement to what previously reported [29]. The latter results suggest that the addition of 4 atom% La³⁺ in the structure of Ce_{0.15}Zr_{0.85}O₂ solid solution increases significantly the strength of the surface basic sites of the material formed, in harmony with the H₂-TPR results (Fig. 4a).

The concentration of surface basic sites (μmol g^{−1}) was obtained by integrating the respective desorption curves up to 700 °C, where no desorption of CO₂ was detected (Fig. 5a). It was found that Zr_{0.93}La_{0.07}O₂ exposes a higher concentration (200.3 μmol g^{−1}) of basic sites compared to Ce_{0.13}Zr_{0.83}La_{0.04}O₂ (179.5 μmol g^{−1}), and which is significantly higher than that of Ce_{0.15}Zr_{0.85}O₂ (66.5 μmol g^{−1}), indicating that addition of 4 atom% La³⁺ in the former solid (keeping practically the same Ce/Zr ratio) enhances significantly its surface basicity. It was reported [77] that the

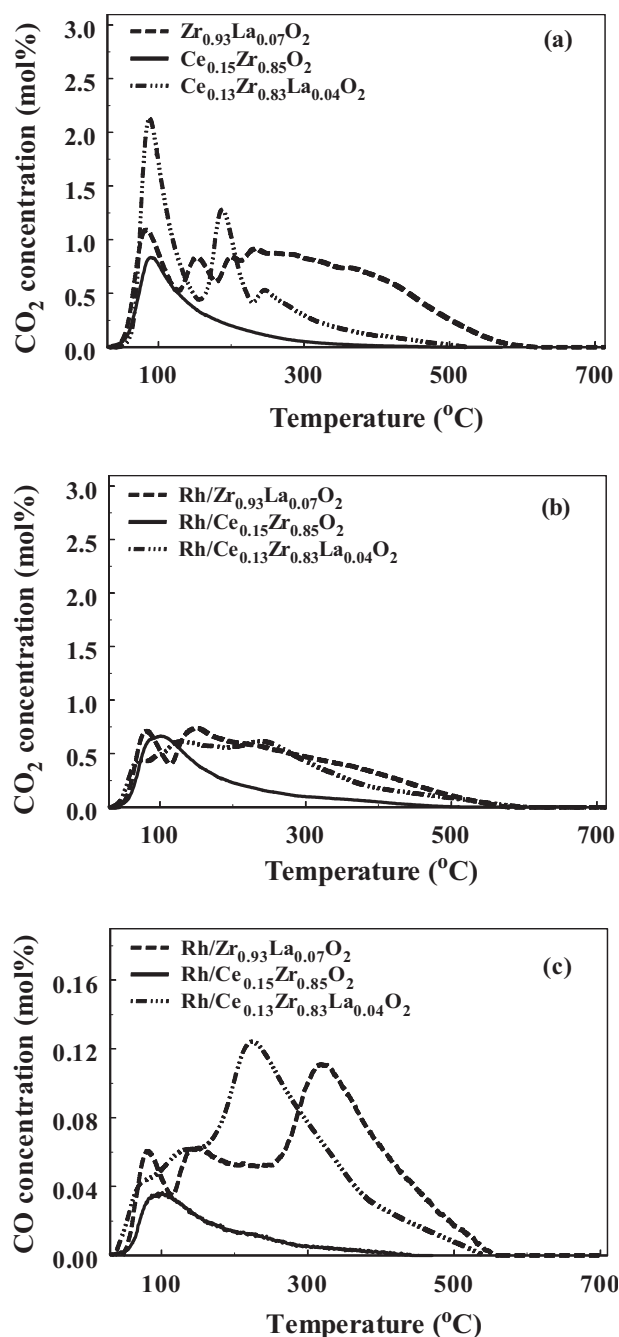


Fig. 5. CO₂-TPD response curves obtained over (a) Zr_{0.93}La_{0.07}O₂, Ce_{0.15}Zr_{0.85}O₂ and Ce_{0.13}Zr_{0.83}La_{0.04}O₂ solids, and (b) 0.5 wt% Rh/Zr_{0.93}La_{0.07}O₂, 0.5 wt% Rh/Ce_{0.15}Zr_{0.85}O₂ and 0.5 wt% Rh/Ce_{0.13}Zr_{0.83}La_{0.04}O₂ solids. (c) TPD response curves of CO formed during CO₂-TPD over the supported-Rh catalysts. Q_{He} = 30 N mL min^{−1}; β = 30 °C min^{−1}; W = 0.5 g.

concentration of surface basic sites can vary with the kind and amount (atom%) of dopant added. The different concentration ($\mu\text{mol g}^{-1}$) and strength of surface basic sites present in each metal oxide support is largely related to the different SSA ($\text{m}^2 \text{g}^{-1}$) and distribution of electron density on the surface lattice oxygen, the latter arising from different local coordination environments of oxygen atoms. It is interesting to note that for the Zr–La–O solid, which showed the largest concentration of CO_2 adsorption ($200.3 \mu\text{mol g}^{-1}$), and after considering a stoichiometry of one carbonate species per two surface oxygen anions on the average, this results in a surface coverage of about 5% for the carbonates formed.

Similar in shape and position CO_2 -TPD response curves (Fig. 5a) were recorded for the corresponding supported-Rh catalysts (Fig. 5b). In this case, CO was also desorbed along with CO_2 , and corresponding traces are shown in Fig. 5c. The observation of linearly adsorbed CO on rhodium (Rh–CO) for the Rh/Ce_{0.13}Zr_{0.83}La_{0.04}O₂ and Rh/Ce_{0.15}Zr_{0.85}O₂ solids following H_2 reduction was confirmed following *in situ* DRIFTS- CO_2 chemisorption studies (Section 3.3.1). At this point it is essential to underline that formation of surface and subsurface oxygen vacancies does occur following reduction of the catalyst [29,79]. The previous remarks suggest that the presence of oxygen vacancies in the support, which were formed during hydrogen reduction, are offered for CO_2 dissociation into CO and lattice oxygen [80]. This reaction step has also been proposed by other researchers in an attempt to study the CO and CO_2 adsorption on CeO₂-containing supported-Rh and -Pt catalysts [29,81]. The CO_2 -TPD response curve obtained for Rh/Zr_{0.93}La_{0.07}O₂ consists of two peaks ($T_M = 83$ and 154°C) accompanied with a large and broad shoulder at the falling part of the high-temperature peak. A single CO_2 desorption peak ($T_M = 106^\circ\text{C}$) with a shoulder on the falling part of it (200 – 500°C) was recorded for Rh/Ce_{0.15}Zr_{0.85}O₂, whereas three CO_2 desorption peaks ($T_M = 71$, 128 and 243°C) appeared for Rh/Ce_{0.13}Zr_{0.83}La_{0.04}O₂. The above CO_2 -TPD results are in agreement with others reported [78,82], and will be further discussed in relation to the *in situ* DRIFTS- CO_2 chemisorption studies performed (Section 3.2.1).

The amount ($\mu\text{mol g}^{-1}$) of CO_2 desorbed from each supported-Rh catalyst follows the order: Rh/Zr_{0.93}La_{0.07}O₂ ($169 \mu\text{mol g}^{-1}$) > Rh/Ce_{0.13}Zr_{0.83}La_{0.04}O₂ ($147.8 \mu\text{mol g}^{-1}$) > Rh/Ce_{0.15}Zr_{0.85}O₂ ($64.8 \mu\text{mol g}^{-1}$), which is similar to the one obtained over the mixed metal oxide supports alone (Table 4). The amount of CO_2 desorbed is found to be lower than that of support alone (Fig. 5a), but the total concentration of equivalent carbon (CO and CO_2) for the support and supported-Rh catalyst is similar to within 10% (Table 4). This deviation is likely to be the result of some reduction expected in the SSA of supported-Rh compared to the support alone, following impregnation, calcination and reduction conditions.

It is observed that the shape and position of CO-TPD response curves (Fig. 5c) are similar to the CO_2 -TPDs (Fig. 5b). On the other hand, the peak maxima in the appearance of CO differ significantly for the three solids. In the case of Rh/Zr_{0.93}La_{0.07}O₂, peaks at 85 , 147 and 325°C were observed, whereas a single CO desorption peak was detected for Rh/Ce_{0.15}Zr_{0.85}O₂ ($T_M = 100^\circ\text{C}$). By increasing the La³⁺ content in the support composition the three CO-TPD peaks shifted to lower temperatures (72 , 127 and 227°C) compared to the case of Rh/Zr_{0.93}La_{0.07}O₂. About 2.5 times lower CO was desorbed when Rh is supported on Ce_{0.15}Zr_{0.85}O₂ compared to the two La-containing supported Rh catalysts (Table 4).

3.1.7. CO chemisorption followed by TPD

Fig. 6a and b present CO and CO_2 TPD response curves, respectively, obtained over the Rh/Zr_{0.93}La_{0.07}O₂, Rh/Ce_{0.15}Zr_{0.85}O₂ and Rh/Ce_{0.13}Zr_{0.83}La_{0.04}O₂ catalysts following CO chemisorption at 25°C . In several supported-Rh catalytic systems, CO desorption is accompanied by a significant production of CO_2 and smaller

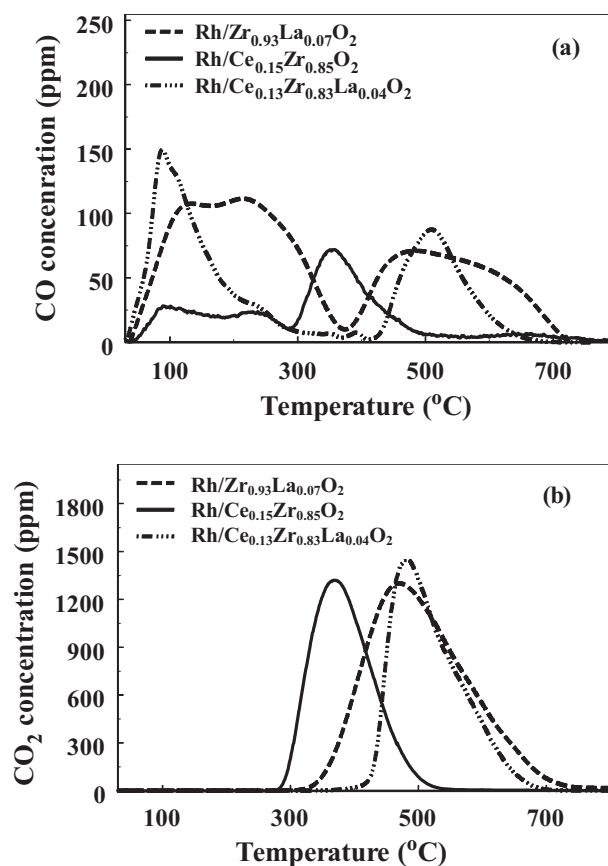
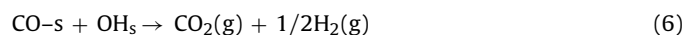


Fig. 6. TPD response curves of CO (a) and CO_2 (b) obtained over the 0.5 wt% Rh/Zr_{0.93}La_{0.07}O₂, 0.5 wt% Rh/Ce_{0.15}Zr_{0.85}O₂ and 0.5 wt% Rh/Ce_{0.13}Zr_{0.83}La_{0.04}O₂ catalysts following CO chemisorption at 25°C . $Q_{\text{He}} = 30 \text{ N mL min}^{-1}$; $\beta = 30^\circ\text{C min}^{-1}$; $W = 0.5 \text{ g}$.

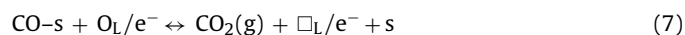
amounts of molecular hydrogen. The formation of CO_2 during CO-TPD could be the result of Boudouard reaction (5):



and reaction of CO with hydroxyl groups of support ($-\text{OH}_\text{L}$) at the metal-support interface, the latter being responsible for the formation of H_2 [29,83,84]:



CO_2 could also be formed by the reaction of adsorbed CO with lattice oxygen located at the metal-support interface, according to reaction (7), where ($\square_\text{L}/\text{e}^-$) presents a lattice surface oxygen vacant site [29,83]:



Reaction (7) was previously found [29] to be responsible for the formation of CO_2 in a larger extent than reaction (5) on a similar supported-Rh catalytic system (0.5 wt%Rh/Ce–Zr–Mg–O). In the present case, no H_2 formation was observed, excluding therefore reaction (6).

As seen in Fig. 6a, all CO-TPD profiles consist mainly of three desorption peaks, two of which are located in the 25 – 300°C range, and one at temperatures higher than 300°C . In particular, in the case of Rh/Zr_{0.93}La_{0.07}O₂ two distinct and a third broad CO desorption peak were observed ($T_M = 128$, 224 and 534°C , respectively), while for the Rh/Ce_{0.15}Zr_{0.85}O₂ and Rh/Ce_{0.13}Zr_{0.83}La_{0.04}O₂ solids, these peaks were recorded at 98 , 230 and 357°C , and 87 , 245 and 512°C , respectively (Table 5). These results imply that at least three kinds of adsorbed CO are formed on the Rh surface in

Table 4
Amounts of desorbed CO and CO₂ (μmol g⁻¹) during CO₂-TPD studies on Zr_{0.93}La_{0.07}O₂, Ce_{0.15}Zr_{0.85}O₂ and Ce_{0.13}Zr_{0.83}La_{0.04}O₂ supports and their corresponding supported-Rh catalysts.

Solid composition	Amount of CO (μmol g ⁻¹)	Amount of CO ₂ (μmol g ⁻¹)	Total (μmol g ⁻¹)
0.5 wt%Rh/Zr _{0.93} La _{0.07} O ₂	20.4	169.0	189.4
0.5 wt%Rh/Ce _{0.15} Zr _{0.85} O ₂	8.4	64.8	73.2
0.5 wt%Rh/Ce _{0.13} Zr _{0.83} La _{0.04} O ₂	19.5	147.8	167.3
Zr _{0.93} La _{0.07} O ₂	–	200.3	200.3
Ce _{0.15} Zr _{0.85} O ₂	–	66.5	66.5
Ce _{0.13} Zr _{0.83} La _{0.04} O ₂	–	179.5	179.5

Table 5
Amounts of desorbed CO and CO₂ (μmol g⁻¹) estimated from CO-TPD studies on supported-Rh catalysts. The peak maximum desorption temperatures (*T_M*) of CO are also given.

Catalyst	<i>T_M</i> (1) (°C)	<i>T_M</i> (2) (°C)	<i>T_M</i> (3) (°C)	CO (μmol g ⁻¹)	CO ₂ (μmol g ⁻¹)	Total (μmol g ⁻¹)
0.5 wt%Rh/Zr _{0.93} La _{0.07} O ₂	128	224	534	3.5	19.6	23.1
0.5 wt%Rh/Ce _{0.15} Zr _{0.85} O ₂	98	230	357	1.0	13.1	14.1
0.5 wt%Rh/Ce _{0.13} Zr _{0.83} La _{0.04} O ₂	87	245	512	2.9	14.4	17.3

accordance with previous results [29]. The CO species desorbing below 400 °C are attributed to linear, gem-dicarbonyl and bridged CO [29]. The high temperature (*T* > 400 °C) desorption of CO is likely to be the result of reaction of atomic carbon formed by the Boudouard reaction (5), which takes place at lower temperatures, with the surface lattice oxygen of support ($C_s + O_L/e^- \rightarrow CO(g) + s + \square_L/e^-$ (oxygen vacant site)). By comparing the CO-TPDs of Rh/Ce_{0.15}Zr_{0.85}O₂ and Rh/Ce_{0.13}Zr_{0.83}La_{0.04}O₂, it is clear that the presence of 4 atom% La³⁺ in the Ce–Zr–La–O support composition leads to a significant increase in the desorption temperature of the strongly bound CO species (*T* > 300 °C). This is also true for the desorbed CO₂ (Fig. 6b). It is noted that CO₂ is produced in a single large peak at temperatures above 300 °C for all catalysts (Fig. 6b). The CO₂-TPD peaks were centered at 448, 480 and 484 °C for the Rh/Ce_{0.15}Zr_{0.85}O₂, Rh/Zr_{0.93}La_{0.07}O₂, and Rh/Ce_{0.13}Zr_{0.83}La_{0.04}O₂, respectively. The quantities of desorbed CO and CO₂ are given in Table 5. In all cases, a significantly larger amount of CO₂ was desorbed compared to CO.

3.1.8. Oxygen storage capacity (OSC) measurements

Table 6 presents OSC and OSCC measurements (μmol O g_{cat}⁻¹) obtained over the supported-Rh catalysts in the 350–550 °C range. In all cases, the OSC and OSCC increased with increasing temperature at which oxygen was stored and reacted off by H₂. It is observed that in the case of Rh/Ce_{0.13}Zr_{0.83}La_{0.04}O₂ both OSC and OSCC quantities were significantly higher for all reaction temperatures compared to the other two solids, where the introduction of 4 atom% La³⁺ in Ce_{0.15}Zr_{0.85}O₂ largely enhanced OSC. For example, at the lowest *T*_{OSC} of 350 °C the OSCC increased by a factor of 1.6, whereas at the highest *T*_{OSC} of 550 °C an increase by a factor of 1.3 was obtained. Similarly, in the case of OSC an increase by a factor of 1.3 and 1.4 was obtained at 350 and 550 °C, respectively (Table 6). According to the work of Vidmar et al. [45], introduction of trivalent cations (e.g., La³⁺, Y³⁺) in CeO₂–ZrO₂ solid solution favours phase homogeneity and improves significantly the OSC even at low temperatures. Similarly, Dai et al. [85] reported the creation of additional defects within the CeO₂–ZrO₂ lattice after Y³⁺ introduction, which resulted in the increase of oxygen mobility. The OSC/OSCC results of Table 6 are in good agreement with the H₂-TPR results of Fig. 4.

3.2. In situ DRIFTS studies

3.2.1. CO₂ chemisorption on Rh/Ce_{0.15}Zr_{0.85}O₂ and Rh/Ce_{0.13}Zr_{0.83}La_{0.04}O₂ solids

It is well known that CO₂ may act as Lewis acid towards basic O²⁻ and –OH surface sites leading to the formation of carbonate

and hydrogen carbonate species, respectively. Fig. 7 compares the DRIFTS spectra recorded in the 1750–1150 cm⁻¹ range (K–M units) after a 30-min exposure to a 3 vol%CO₂/He gas mixture at 450 °C over the Rh/Ce_{0.13}Zr_{0.83}La_{0.04}O₂ and Rh/Ce_{0.15}Zr_{0.85}O₂ solids. The spectra obtained after deconvolution and curve fitting (Section 2.4.1) are also shown. In the case of Rh/Ce_{0.13}Zr_{0.83}La_{0.04}O₂, the IR band shown at 1505 cm⁻¹ corresponds to the OCO_{as} vibrational mode of unidentate carbonate (CO₃²⁻), whereas the broad IR band at 1567 cm⁻¹ to the OCO_{as} vibrational mode of formate and bidentate carbonate [86,87,88]. The formation of the latter species is favoured at high adsorption temperatures [39,40]. The IR band recorded at 1404 cm⁻¹ is assigned to the OCO_s of unidentate carbonate, while the low-wavelength band recorded at 1325 cm⁻¹ could potentially be assigned to the OCO_s of bidentate formate [87,88]. The observation of well defined IR bands in the spectral region of 2900–2800 cm⁻¹ (not shown) corresponding to the νC–H vibrational mode of formate species confirmed the latter assignment and that for the IR band at 1567 cm⁻¹. Formate species are formed by the interaction of CO₂ or CO with surface hydroxyl groups of metal oxides. The development of negative bands in the νOH region of 3600–3400 cm⁻¹ (not shown) confirms the latter, in harmony also with previous studies [29]. In the case of Rh/Ce_{0.15}Zr_{0.85}O₂ (Fig. 7), all the above mentioned IR bands were detected at slightly shifted wavenumbers. It is also noted the formation of linearly adsorbed CO (Rh–CO) (IR band centered at 1980 cm⁻¹, not shown) in both catalysts. The DRIFTS–CO₂

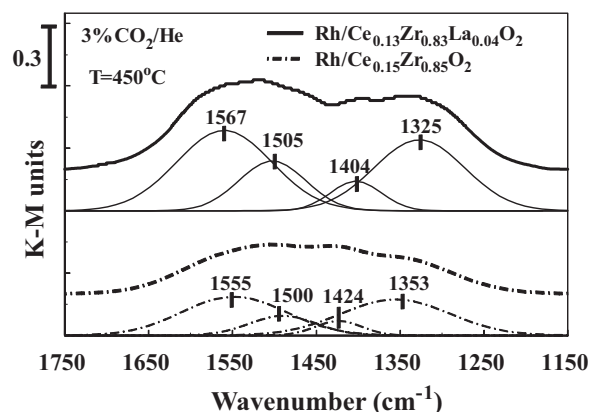


Fig. 7. In situ DRIFTS spectra recorded in the 1750–1150 cm⁻¹ range (K–M units) over the Rh/Ce_{0.13}Zr_{0.83}La_{0.04}O₂ and Rh/Ce_{0.15}Zr_{0.85}O₂ catalysts after a 30-min exposure to a 3 vol%CO₂/He gas mixture at 450 °C. Deconvoluted spectra are also shown (lower part).

Table 6OSC and OSCC ($\mu\text{mol O g}_{\text{cat}}^{-1}$) measured in the 350–550 °C range over the supported-Rh catalysts investigated.

Catalyst	T (°C)	OSC ($\mu\text{mol O g}_{\text{cat}}^{-1}$)	OSCC ($\mu\text{mol O g}_{\text{cat}}^{-1}$)
0.5 wt% Rh/Zr _{0.93} La _{0.07} O ₂	350	101	135
	400	112	136
	450	117	148
	550	140	180
0.5 wt% Rh/Ce _{0.15} Zr _{0.85} O ₂	350	288	354
	400	309	397
	450	328	472
	550	365	615
0.5 wt% Rh/Ce _{0.13} Zr _{0.83} La _{0.04} O ₂	350	368	577
	400	402	590
	450	436	662
	550	524	773

chemisorption results for Rh/Ce_{0.13}Zr_{0.83}La_{0.04}O₂ (Fig. 7) previously discussed is in harmony with the TPD-CO₂ results (Fig. 5), where three CO₂ desorption peaks were evident. In the case of Rh/Ce_{0.15}Zr_{0.85}O₂, a single but broad CO₂ desorption peak was observed (Fig. 5), which could be seen as the result of at least two CO₂ desorption states.

The increase by a factor of two of the integral band area corresponding to formate species, and the increase in the relative population of formate *versus* carbonates after the introduction of La³⁺ in the catalyst support composition should be noted. This may have a direct consequence on the rate of WGS reaction if formate might be considered as an active reaction intermediate and carbonates as inactive ones, the latter competing with water for chemisorptions sites. This fact was recently reported to be true for the WGS at 300 °C on Pt supported on ceria [89,90].

3.2.2. Water chemisorption on Rh/Ce_{0.15}Zr_{0.85}O₂ and Rh/Ce_{0.13}Zr_{0.83}La_{0.04}O₂ catalysts

Fig. 8a compares the DRIFTS spectra recorded in the 3800–3000 cm^{−1} range (K–M units) for the Rh/Ce_{0.13}Zr_{0.83}La_{0.04}O₂ and Rh/Ce_{0.15}Zr_{0.85}O₂ catalysts after a 30-min exposure to the 40 vol% H₂O/He gas mixture at 450 °C. A broad IR band is observed for both catalysts illustrating that –OH groups are formed upon water interaction. According to the literature [86,91], the formation of surface hydroxyls is a result of water dissociation on the surface of a metal oxide (Mⁿ⁺–O^{n−}), where surface oxygen anion (O^{n−}) becomes bonded to the hydrogen atom of water, and at the same time the OH group becomes bonded to the top of an adjacent metal cation (free hydroxyl). The free hydroxyl groups proved to be of several distinct types, the number of which depending on the surface oxygen local coordination [91,92]. The latter has the consequence to the large broadening of the νO–H region depicted in Fig. 8a. Moreover, H-bonding between adjacent surface M–OH species or between M–OH and water at high surface coverages also results in the broadening of the recorded νO–H stretching IR band [86]. The H-bonded hydroxyls are characterized by lower frequencies (<3500 cm^{−1}) [93]. Daturi et al. [94] and Ouyang et al. [93] studied the vibrational modes of –OH species on the surface of Ce_xZr_{1−x}O₂ solid solution using *in situ* FTIR after oxidation and reduction procedures at 400 °C. They reported changes in νO–H stretching in the region 3800–3500 cm^{−1}, where free hydroxyls are formed. Based on these results [94], the latter species are coordinated only to cerium metal cations.

In order to identify the effect of La³⁺ addition in the Ce–Zr–O support composition on the distribution of the different kinds of free –OH species formed on the surface of Rh/Ce_{0.13}Zr_{0.83}La_{0.04}O₂, the DRIFTS spectra shown in Fig. 8a were deconvoluted in the region 3800–3500 cm^{−1}, and the obtained results are shown in Fig. 8b. Three well defined IR bands at 3716, 3663 and 3600 cm^{−1} (Ce_{0.15}Zr_{0.85}O₂) assigned to mono-coordinated OH (I) (1-fold coordinated), doubly bridging (II) (2-fold coordinated), and

triply bridging OH (III) (3-fold coordinated) species, respectively, are obtained, in excellent agreement with results reported on Ce_xZr_{1−x}O₂ and CeO₂ surfaces [93,94,95]. The three different kinds of free –OH species is suggested to be associated with cerium cations due to the small surface atom% composition of La³⁺ (XPS studies, Table 3).

By comparing the deconvoluted IR bands of Rh/Ce_{0.15}Zr_{0.85}O₂ and Rh/Ce_{0.13}Zr_{0.83}La_{0.04}O₂ (Fig. 8b), the clear shift in the IR bands of the 2-fold and 3-fold coordinated –OH groups towards lower wavenumbers was caused by the presence of La³⁺ in the Ce–Zr–O support. Also, the % population of the latter two kinds of –OH groups (type II and III) was increased in the case of Ce–Zr–La–O compared to Ce–Zr–O support. It has been reported [96,97] that the bridging type II and III –OH groups act as weakly acidic Brønsted sites with an acid strength increasing with decreasing O–H stretching

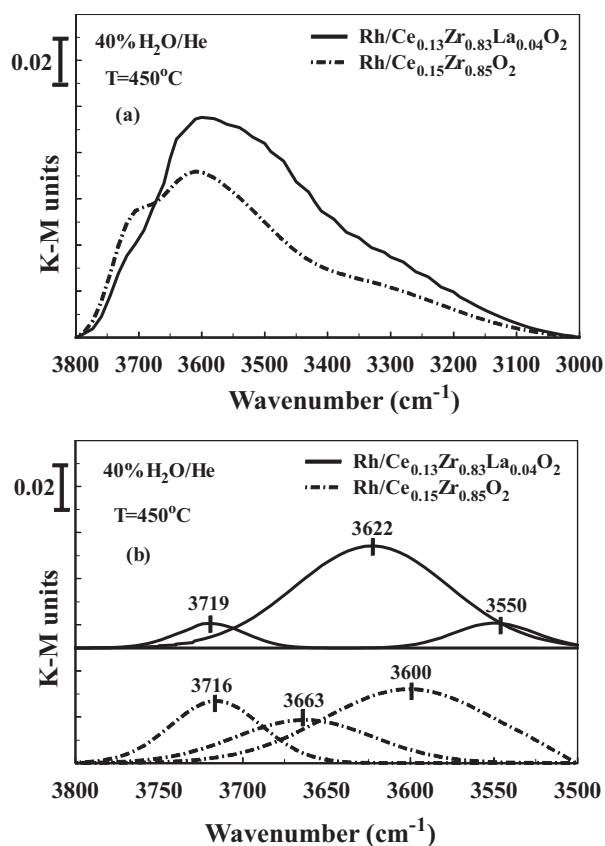


Fig. 8. (a) *In situ* DRIFTS spectra recorded in the 3800–3000 cm^{−1} range (K–M units) over the Rh/Ce_{0.13}Zr_{0.83}La_{0.04}O₂ and Rh/Ce_{0.15}Zr_{0.85}O₂ catalysts after a 30-min exposure to a 40 vol% H₂O/He gas mixture at 450 °C. (b) Deconvoluted DRIFTS spectra shown in (a) in the 3800–3500 cm^{−1} region.

wavenumber. These –OH groups interact with CO via H-bonding, which could lead to the formation of HCOO– (formate) species. It was recently demonstrated *via operando* SSTIKA-MS-DRIFTS studies [89,90] that at 300 °C formate species becomes an active intermediate in the WGS reaction over Pt/CeO₂ catalysts, whereas it becomes inactive at lower temperatures. Since the WGS reaction is part of the network of reactions in steam reforming, the former adjusting the overall H₂-yield, it is suggested that the presence of La³⁺ in the Ce–Zr–La–O support could play a role in the H₂ production *via* steam reforming of phenol by enhancing the concentration of active –OH (type II and III) groups in the support. This issue is further elaborated in Section 3.4.

3.3. Catalytic performance of supported-Rh

Fig. 9a–c present the effect of reaction temperature on phenol conversion, X_p (%), hydrogen product concentration (mol%, dry basis) and H₂-yield, Y_{H_2} (%), and CO/CO₂ product ratio, respectively, obtained over the Rh/Zr_{0.93}La_{0.07}O₂, Rh/Ce_{0.15}Zr_{0.85}O₂, Rh/Ce_{0.13}Zr_{0.83}La_{0.04}O₂, and a commercial Ni-based catalyst (44 wt% NiO/ γ -Al₂O₃, Sud-Chemie, code C11-PR). The latter catalyst is used for “tars” steam reforming. The activity in terms of phenol conversion and H₂ production obtained at 400 and 450 °C over the supports alone is also presented (Fig. 9a and b). The Rh/Ce_{0.13}Zr_{0.83}La_{0.04}O₂ catalyst exhibits the highest values in terms of phenol conversion in the 350–500 °C range (Fig. 9a), and the order of catalytic activity obtained is: Rh/Ce_{0.13}Zr_{0.83}La_{0.04}O₂ > Rh/Zr_{0.93}La_{0.07}O₂ > Rh/Ce_{0.15}Zr_{0.85}O₂ ~ Ni-based (C11-PR). At the lowest T of 350 °C and the highest one of 550 °C, all catalysts showed small differences in their activity. On the other hand, at 400 °C the Rh/Ce_{0.13}Zr_{0.83}La_{0.04}O₂ exhibits approximately 54% higher phenol conversion compared to the Ni-based industrial catalyst. It should be pointed out that the commercial catalyst has a Ni loading of 44 wt% to be compared to 0.5 wt% of Rh used in the present supported-Rh catalysts. It should be also noted that the Ni-based catalyst results reported in Fig. 9 were obtained after using the same amount of catalyst and GHSV as in the case of supported-Rh catalysts.

By comparing the activity of supported-Rh and that of support alone, it is more than clear that the activity of supported-Rh is largely due to the presence of Rh metal. In addition, the order of activity parallels that of Rh metal particle size, suggesting that the phenol steam reforming activity (per gram of catalyst basis) over the present supported-Rh catalysts is favoured over small Rh particles, the formation of which depending on the support chemical composition. These remarks are in full agreement with our previous reported results over Ce–Zr–Mg–O mixed metal oxides-supported Rh catalysts [29]. On the other hand, integral TOF_{H₂} (s^{−1}) values estimated at 400 °C for the three supported-Rh catalysts (Fig. 9b) reveal that Rh/Ce_{0.15}Zr_{0.85}O₂ and Rh/Ce_{0.13}Zr_{0.83}La_{0.04}O₂ have similar turnover frequencies (1.05/1.15 s^{−1}), whereas the Rh/Zr_{0.93}La_{0.07}O₂ catalyst has a slightly larger value (1.22 s^{−1}). However, it should be rather questionable to draw conclusions on the structure sensitivity of the steam reforming of phenol reaction on the present supported-Rh catalysts based on the TOF_{H₂} (s^{−1}) values, since this assumes that the rate-limiting step of the reaction is associated with the Rh surface only, which is very likely not to be the case [98,99,100] as discussed below.

The hydrogen product concentration (mol%) and yield were found to exhibit a similar to the phenol conversion *versus* temperature profile. At 450 °C, approximately 80% of the maximum hydrogen production was achieved over the Rh/Ce_{0.13}Zr_{0.83}La_{0.04}O₂ catalyst, and only 55% over the commercial Ni-based catalyst, in good agreement with what has been reported for the steam reforming of “tars” [21,22,25,26,101,102]. Moreover, a recent review on the catalytic conditioning of biomass-derived “syngas” [103]

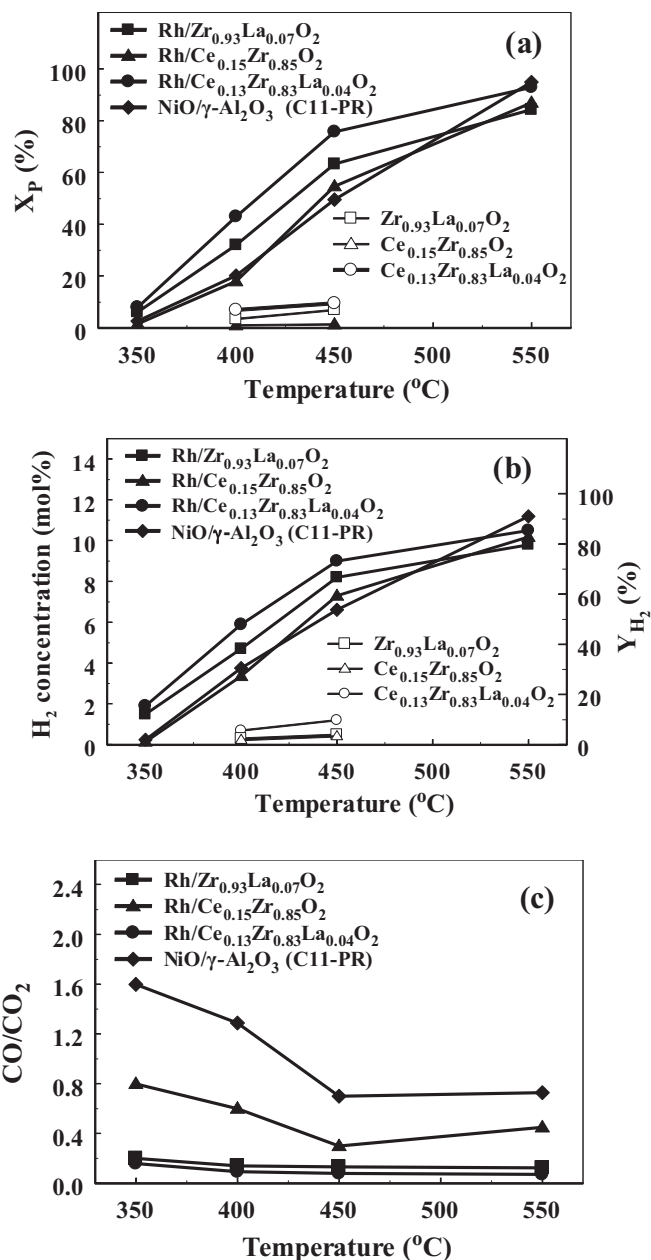


Fig. 9. Dependence of (a) phenol conversion, X_p (%), (b) hydrogen product concentration (mol% dry-basis) and H₂-yield (%), and (c) CO/CO₂ gas product ratio on reaction temperature for the 0.5 wt% Rh/Zr_{0.93}La_{0.07}O₂, 0.5 wt% Rh/Ce_{0.15}Zr_{0.85}O₂, 0.5 wt% Rh/Ce_{0.13}Zr_{0.83}La_{0.04}O₂ and commercial Ni-based catalysts. Corresponding results for the supports alone are also shown in (a) and (b). Feed composition: 0.6 vol% C₆H₅OH/40 vol% H₂O/59.4 vol% He; W_{cat} = 0.3 g; F_T = 200 mL min^{−1}; GHSV = 54,000 h^{−1}.

showed that Rh, Ni and Pt emerged as the best potential base metals for use in steam reforming, with Rh being highly resistant to coke than most of the other metals studied. Furthermore, selected studies on ethanol steam reforming using noble metal catalysts [20,21,22,23,104,105,106] led to the conclusion that Rh is generally more effective than other noble metals, such as Pt, Pd and Au towards hydrogen production. CeO₂, MgO and La₂O₃ were also identified as suitable supports for efficient ethanol reforming on Rh [20,107]. Moreover, La³⁺ addition in Ce–Zr–O solids was previously mentioned to improve syngas selectivity [108]. The previous statements are in good agreement with the present activity results (Fig. 9a and b), where small amounts of La³⁺ (4 and 7 atom%) introduced in Ce–Zr–O solid solution matrix led to

significant improvements in phenol steam reforming activity, when 0.5 wt% Rh was loaded on them. It is suggested that the substantially higher support basicity of both La-containing-supported Rh catalysts probed by the CO₂-TPDs (Fig. 5b) are largely responsible for the enhanced catalytic activity observed (Fig. 9a and b) as explained in what follows.

According to the mechanism described for toluene steam reforming [109,110], both *metal and support* play an essential role in the catalytic behaviour of supported-Rh, -Pd, and -Pt catalysts. In this *bi-functional mechanism* the aromatic molecule is dissociated on the metal particle leading to adsorbed hydrocarbon fragments, whereas the water molecule is activated on the support. The resulting hydroxyl groups migrate to the metal particles through the metal/support interface which react with hydrocarbon fragments towards CO, CO₂ and H₂ formation. This mechanism was later supported by Polychronopoulou et al. [98,99,100] in the case of steam reforming of phenol over supported-Rh and Fe catalysts, with similar supports as the ones used in the present work, after performing transient ¹⁸O and deuterium isotopic experiments. Along these lines, the increased surface basicity of La³⁺-doped mixed metal oxides (Fig. 5) enhances water dissociation, thus formation of -OH species, in harmony with the *in situ* DRIFTS-H₂O chemisorption studies previously mentioned and discussed (Section 3.2.2). CO₂-TPDs (Fig. 5) revealed that La³⁺-doped catalysts exhibited moderate and strong basic sites to a significantly larger concentration than the Rh/Ce_{0.15}Zr_{0.85}O₂ solid. Both kinds of basic sites favour dissociation of water (Section 3.2.2). The superior performance of Rh/Ce_{0.13}Zr_{0.83}La_{0.04}O₂ in terms of OSC/OSCC in the 350–550 °C range relates to its superior catalytic activity performance (Fig. 9a and b) having considered at the same time the essential mechanistic aspects of the phenol steam reforming as outlined above.

Based on the above-offered discussion, it could be concluded that the superior reforming activity of Rh/Ce_{0.13}Zr_{0.83}La_{0.04}O₂ is related to the enhanced rate of the rate-limiting step of the bi-functional mechanism, which is likely to be associated with support surface active sites. It is suggested that the rates of important steps associated with the support are influenced in a positive way by the enhanced surface *basicity* and *oxygen mobility* in terms of both concentration and reactivity, but also by the presence of *small Rh particles*. This behaviour is clearly triggered by the presence of La³⁺ in the Ce–Zr–La–O solid solution matrix.

The La-containing-supported Rh catalysts were also found to exhibit a significantly lower CO/CO₂ product ratio among the other catalysts (Fig. 9c). This could also suggest the significant effect of support chemical composition on the rates of reactions (1) and (2) which control the overall H₂, CO and CO₂ product yields. The facts that the Ce_{0.13}Zr_{0.83}La_{0.04}O₂-supported Rh exhibits the lowest CO/CO₂ product ratio (Fig. 9c), and at the same time the largest H₂ product yield (Fig. 9b), strongly support the view that this particular support composition largely promotes the water-gas shift reaction (2) as also evidenced in the present work (Section 3.4). The effect of support on the CO/CO₂ product ratio was one of the main observations of Digne et al. [21,22] for the steam reforming of ethanol over 2 wt% Rh supported on CeO₂, ZrO₂ and CeO₂–ZrO₂ (Ce/Zr = 4, 2, and 1) in the 300–500 °C range. A dramatic influence of catalyst support composition on the CO/CO₂ product ratio was reported [21,22], with CeO₂–ZrO₂ being the best support.

It is instructive to show here how close to equilibrium the WGS reaction was at the exit stream of the reactor. In the case of Rh/Ce_{0.13}Zr_{0.83}La_{0.04}O₂ for the phenol steam reforming at 350 °C, using $y_{H_2} = 0.019$, $y_{CO_2} = 0.0039$, $y_{CO} = 0.0039$ and $y_{H_2O} = 0.4$ (y_i = mole fraction of gaseous species), and considering that the theoretical equilibrium constant, $K_{WGS,th}$ equals to 20.45, it is estimated that the theoretical product $y_{CO_2} \cdot y_{H_2}$

equals to 50.7×10^{-4} , while the corresponding experimental value is only 7.36×10^{-4} . Similarly, at 550 °C it was found that the theoretical product $y_{CO_2} \cdot y_{H_2}$ equals to 44.3×10^{-4} , while the corresponding experimental value is 46.5×10^{-4} ($K_{WGS,th} = 3.43$; $y_{H_2} = 0.105$; $y_{CO_2} = 0.0443$; $y_{CO} = 0.0032$; $y_{H_2O} = 0.4$). These results clearly demonstrate that under the experimental conditions examined, the WGS reaction was far from being at equilibrium at 350 °C but very close to that at 550 °C.

A long-term (12 h on stream) catalyst's stability test was performed at 550 °C (0.6% C₆H₅OH/40% H₂O/He; 54,000 h⁻¹) over the 0.5 wt% Rh/Ce_{0.13}Zr_{0.83}La_{0.04}O₂ solid. A drop in the H₂ production (Fig. 9b, 30 min on stream) by only 5% after 12 h on stream was observed, similar to the case of 0.5 wt% Rh/Ce_{0.14}Zr_{0.81}Mg_{0.05}O₂ catalyst [29]. An on-going research work in our laboratory currently investigates the presence of CH₄, CO₂, CO and H₂ ("biosyngas") in the C₆H₅OH/H₂O/He feed gas composition on the performance of the same supported-Rh catalysts. Thus, the present work will be used to establish the role of CH₄, CO₂, CO and H₂ on the phenol conversion into CO_x ($x = 1, 2$) and H₂.

3.4. Operando DRIFTS-mass spectrometry WGS reaction studies

The kinetic rates of H₂ production during WGS in the presence or absence of H₂ in the feed for the Rh/Ce_{0.15}Zr_{0.85}O₂ and Rh/Ce_{0.13}Zr_{0.83}La_{0.04}O₂ catalysts were estimated *via operando* studies in the DRIFTS reactor cell (Section 2.4.2). A kinetic rate of 3.5 and 5.0 μmol H₂ g⁻¹ s⁻¹, respectively was found after 30-min exposure of the Rh/Ce_{0.15}Zr_{0.85}O₂ and Rh/Ce_{0.13}Zr_{0.83}La_{0.04}O₂ catalysts in the 1%CO/40%H₂O/He (WGS reaction) feed stream. After introducing 7 vol% H₂ in the WGS feed stream (1%CO/40%H₂O/7%H₂/He), a decrease in the kinetic rate of H₂ production by a factor of 1.7 and 1.1 was observed for the Rh/Ce_{0.15}Zr_{0.85}O₂ and Rh/Ce_{0.13}Zr_{0.83}La_{0.04}O₂ catalysts, respectively. These results illustrate the strong retarding effect of hydrogen towards the WGS activity, suggesting a negative reaction order with respect to H₂ in agreement with results reported [44,111]. It is also seen that La-containing-supported Rh exhibits significantly higher WGS activity than Rh/Ce_{0.15}Zr_{0.85}O₂ (an increase by about 40%). As mentioned earlier, since the WGS reaction is part of the network of phenol steam reforming, the above results provide a clue that the increased activity of phenol steam reforming in terms of H₂-yield over Rh/Ce_{0.13}Zr_{0.83}La_{0.04}O₂ (Fig. 9b) is partly due to the positive influence of La³⁺ on the WGS activity. The lower CO/CO₂ product ratio reported (Fig. 9c) points also towards the latter conclusion.

Based on the DRIFTS results obtained (not shown here), the influence of La³⁺ on the relative population of adsorbed reaction intermediates of WGS was as follows:

- A significant increase in the surface concentration of bridged formate species; increase of the integral band area (K–M units) in the 3100–2800 cm⁻¹ region.
- A significant variation in the relative population of the two kinds of adsorbed formate as evidenced by the shape and relative position of the corresponding IR bands.
- The presence of H₂ in the WGS reaction feed stream influenced only slightly the surface coverage of adsorbed linear CO on Rh (Ce_{0.13}Zr_{0.83}La_{0.04}O₂ support), as opposed to the case of Ce_{0.15}Zr_{0.85}O₂ support. This is an important result which supports the observed increased WGS and phenol steam reforming activities (Section 3.3).

4. Conclusions

The following conclusions can be considered from the results of the present work:

- (a) Introduction of 4 atom% La^{3+} in the $\text{Ce}_{0.15}\text{Zr}_{0.85}\text{O}_2$ solid solution matrix was found to enhance Rh dispersion, surface reducibility, surface basicity, and oxygen storage capacity for the $\text{Rh}/\text{Ce}_{0.13}\text{Zr}_{0.83}\text{La}_{0.04}\text{O}_2$ compared to $\text{Rh}/\text{Ce}_{0.15}\text{Zr}_{0.85}\text{O}_2$ solid.
- (b) CO_2 -TPD studies over pre-reduced (H_2 , $200^\circ\text{C}/2\text{ h}$) $\text{Rh}/\text{Zr}_{0.93}\text{La}_{0.07}\text{O}_2$, $\text{Rh}/\text{Ce}_{0.15}\text{Zr}_{0.85}\text{O}_2$ and $\text{Rh}/\text{Ce}_{0.13}\text{Zr}_{0.83}\text{La}_{0.04}\text{O}_2$ catalysts led to CO desorption along with CO_2 due to the dissociation of the latter on surface oxygen vacancies, which were strongly dependent on support chemical composition. These results were in agreement with those obtained in the *in situ* DRIFTS- CO_2 chemisorption studies at 450°C .
- (c) Phenol steam reforming performed in the 350 – 550°C range is largely promoted by the presence of small amounts of La^{3+} in the Ce–Zr–O solid solution used as support of 0.5 wt% Rh metal.
- (d) A 0.5 wt% $\text{Rh}/\text{Ce}_{0.13}\text{Zr}_{0.83}\text{La}_{0.04}\text{O}_2$ catalyst developed led to a significantly better performance towards steam reforming of phenol in the 350 – 450°C range in terms of phenol conversion, H_2 -yield and CO/CO_2 product ratio compared to a commercial Ni-based catalyst (44 wt% Ni).
- (e) *In situ* DRIFTS- H_2O chemisorption studies conducted over the pre-oxidized $\text{Rh}/\text{Ce}_{0.15}\text{Zr}_{0.85}\text{O}_2$ and $\text{Rh}/\text{Ce}_{0.13}\text{Zr}_{0.83}\text{La}_{0.04}\text{O}_2$ solids revealed the population of three different kinds of –OH groups. The presence of La^{3+} in the support composition resulted in the increase of population of the 2-fold and 3-fold coordinated –OH groups characterized by more Brønsted acidic character than the 1-fold coordinated –OH groups.
- (f) The kinetic rate of H_2 production *via* the WGS reaction over the $\text{Rh}/\text{Ce}_{0.13}\text{Zr}_{0.83}\text{La}_{0.04}\text{O}_2$ was found to be $5.0\ \mu\text{mol g}^{-1}\text{ s}^{-1}$, which is about 1.4 times larger than that obtained on the $\text{Rh}/\text{Ce}_{0.15}\text{Zr}_{0.85}\text{O}_2$ catalyst. The latter result partly contributes to the positive influence of La^{3+} towards the steam reforming of phenol activity.
- (g) The strong retarding effect of hydrogen towards WGS activity was illustrated. This effect was minimized in the presence of La^{3+} (0.5 wt% $\text{Rh}/\text{Ce}_{0.13}\text{Zr}_{0.83}\text{La}_{0.04}\text{O}_2$), in harmony with its positive effect on the overall reforming of phenol activity towards H_2 formation.

Acknowledgement

The financial support of the Cyprus Research Promotion Foundation (project ΠENEK/ENIΣX/0308/51) and the Research Committee of the University of Cyprus is gratefully acknowledged. The authors also thank MEL Chemicals (UK) for providing the commercial catalyst support materials ($\text{Zr}_{0.93}\text{La}_{0.07}\text{O}_2$, $\text{Ce}_{0.15}\text{Zr}_{0.85}\text{O}_2$ and $\text{Ce}_{0.13}\text{Zr}_{0.83}\text{La}_{0.04}\text{O}_2$).

References

- [1] N.Z. Muradou, T.N. Veziroğlu, *Int. J. Hydrogen Energy* 33 (2008) 6804.
- [2] S. Zinoviev, F. Müller-Langer, P. Das, N. Bertero, P. Fornasiero, M. Kaltschmitt, G. Centi, S. Miertsch, *ChemSusChem* 3 (2010) 1106.
- [3] C. Koroneos, A. Dompas, G. Roubas, *Chem. Eng. Proc.* 47 (2008) 1261.
- [4] J.N. Armor, *Catal. Lett.* 3–4 (2005) 131.
- [5] NRC report, *The Hydrogen Economy: Opportunities, Costs, Barriers, and R&D Needs*, The National Academies Press, 2004.
- [6] R.C. Saxena, D. Seal, S. Kumar, H.B. Goyal, *Ren. Sustain. Energy Rev.* 12 (2008) 1909.
- [7] (a) B.M. Güell, I.V. Babich, L. Lefferts, K. Seshan, *Appl. Catal. B: Environ.* 106 (2011) 280;
(b) W. Torres, S.S. Pansare, J.G. Goodwin, *Cat. Rev.* 49 (2007) 407.
- [8] G.W. Huber, A. Corma, *Angew. Chem. Int. Ed.* 46 (2007) 7184.
- [9] T.A. Milne, N. Abatzoglou, R.J. Evans, *Biomass gasifier tars: their nature, formation and conversion*, NREL/TP-570-25357, National Renewable Energy Laboratory, USA, 1989.
- [10] L. Devi, K.J. Ptasinski, F.J.J.G. Janssen, *Biomass Bioenergy* 24 (2003) 125.
- [11] C.M. Kinoshita, Y. Wang, J. Zhou, *J. Anal. Appl. Pyrol.* 29 (1994) 169.
- [12] European Project, 6th FP, No. 5183309 (SE56), *Biomass Fluidized bed gasification with in situ hot gas cleaning*, 2006–2009.
- [13] L. Devi, K.J. Ptasinski, F.J.J.G. Janssen, S.V.B. van Paasen, P.C.A. Bergman, J.H.A. Kiel, *Renew. Energy* 30 (2005) 565.
- [14] P. Morf, P. Hasler, T. Nussbaumer, *Fuel* 81 (2002) 843.
- [15] D. Wang, D. Montané, E. Chornet, *Appl. Catal. A: Gen.* 143 (1996) 245.
- [16] C. Li, K. Suzuki, *Renewable, Sustain. Energy Rev.* 13 (2009) 594.
- [17] D. Trimm, *Catal. Today* 49 (1999) 3.
- [18] E.C. Vagia, A.A. Lemonidou, *J. Catal.* 269 (2010) 388.
- [19] L. Garcia, R. French, S. Czernik, E. Chornet, *Appl. Catal. A: Gen.* 201 (2000) 225.
- [20] M. Ni, D.Y.C. Leung, M.K.H. Leung, *Int. J. Hydrogen Energy* 32 (2007) 3238.
- [21] C. Diagne, H. Idriss, K. Pearson, M.A. Gómez-García, A. Kiennemann, C.R. Chim. 7 (2004) 617.
- [22] C. Diagne, H. Idriss, A. Kiennemann, *Catal. Commun.* 3 (2002) 565.
- [23] C. Rioche, S. Kulkarni, F.C. Meunier, J.P. Breen, R. Burch, *Appl. Catal. B: Environ.* 61 (2005) 130.
- [24] T. Montini, L. De Rogatis, V. Gombac, P. Fornasiero, M. Graziani, *Appl. Catal. B: Environ.* 71 (2007) 125.
- [25] M. Asadullah, K. Tomishige, K. Fujimoto, *Catal. Commun.* 2 (2001) 63.
- [26] M. Asadullah, T. Miyazawa, S. Ito, K. Kumimori, K. Tomishige, *Energy Fuel* 17 (2003) 842.
- [27] M. Asadullah, S. Ito, K. Kumimori, M. Yamada, K. Tomishige, *J. Catal.* 208 (2002) 255.
- [28] M. Asadullah, T. Miyazawa, S. Ito, K. Kumimori, M. Yamada, K. Tomishige, *Appl. Catal. A: Gen.* 255 (2003) 169.
- [29] D.A. Constantinou, A.M. Efstathiou, *Appl. Catal. B: Environ.* 96 (2010) 276.
- [30] K. Polychronopoulou, J.L.G. Fierro, A.M. Efstathiou, *J. Catal.* 228 (2004) 417.
- [31] K. Polychronopoulou, C.N. Costa, A.M. Efstathiou, *Appl. Catal. A: Gen.* 272 (2004) 37.
- [32] K. Polychronopoulou, K. Giannakopoulos, A.M. Efstathiou, *Appl. Catal. B: Environ.* 111–112 (2012) 360.
- [33] C.N. Costa, T. Anastasiadou, A.M. Efstathiou, *J. Catal.* 194 (2000) 250.
- [34] J.R. Anderson, K.C. Pratt, *Introduction to Characterization and Testing of Catalysts*, Academic Press, New York, 1985.
- [35] A.L. Patterson, *Phys. Rev.* 56 (1939) 978.
- [36] C.D. Wagner, L.E. Davis, M.V. Zeller, J.A. Taylor, R.H. Raymond, L.H. Gale, *Surf. Int. Anal.* 3 (1981) 211.
- [37] P.S. Lambrou, C.N. Costa, S.Y. Christou, A.M. Efstathiou, *Appl. Catal. B: Environ.* 54 (2004) 237.
- [38] C.N. Costa, S.Y. Christou, G. Georgiou, A.M. Efstathiou, *J. Catal.* 219 (2003) 259.
- [39] D.A. Constantinou, A.M. Efstathiou, *Catal. Today* 143 (2009) 17.
- [40] D.A. Constantinou, J.L.G. Fierro, A.M. Efstathiou, *Appl. Catal. B: Environ.* 90 (2009) 347.
- [41] B.C. Smith, *Fundamentals of Fourier Transform Infrared Spectroscopy*, CRC Press, Boca Raton, 1996.
- [42] F.M. Hoffmann, *Surf. Sci. Rep.* 3 (1983) 107.
- [43] G.G. Olympiou, C.M. Kalamaras, C.D. Zeinalipour-Yazdi, A.M. Efstathiou, *Catal. Today* 127 (2007) 304 (and references therein).
- [44] C.M. Kalamaras, P. Panagiotopoulou, D.I. Kondarides, A.M. Efstathiou, *J. Catal.* 264 (2009) 117 (and references therein).
- [45] P. Vidmar, P. Fornasiero, J. Kašpar, G. Gubitosa, M. Graziani, *J. Catal.* 171 (1997) 160.
- [46] B. Yue, R. Zhou, Y. Wang, X. Zheng, *Appl. Catal. A: Gen.* 295 (2005) 31.
- [47] J.D.A. Bellido, E.M. Assaf, *Appl. Catal. A: Gen.* 352 (2009) 179.
- [48] A. Dwivedi, A.N. Cormack, *Phylos. Mag.* 7 (1990) 1.
- [49] K.S. Mazdiyasi, C.T. Lynch, J.S. Smith, *J. Am. Ceram. Soc.* 50 (10) (1967) 532.
- [50] T. Montini, A. Speghini, L. De Rogatis, B. Lorenzuti, M. Bettinelli, M. Graziani, P. Fornasiero, *J. Am. Chem. Soc.* 131 (2009) 13155.
- [51] L.N. Ikryannikova, A.A. Aksenov, G.L. Markaryan, G.P. Muraveva, B.G. Kostyuk, A.N. Kharlanov, E.V. Lunina, *Appl. Catal. A: Gen.* 210 (2001) 225.
- [52] P. Papavasiliou, A. Tsetsekou, V. Matsouka, M. Konsolakis, I.V. Yentekakis, N. Boulos, *Appl. Catal. B: Environ.* 90 (2009) 347.
- [53] M. Ferrandon, T. Krause, *Appl. Catal. A: Gen.* 311 (2006) 135.
- [54] F. Oudet, A. Vejux, P. Courtine, *Appl. Catal.* 50 (1989) 79.
- [55] M. Kawai, M. Uda, M. Ichikawa, *J. Phys. Chem.* 89 (1985) 1654.
- [56] D.I. Kondarides, Z. Zhang, X.E. Verykios, *J. Catal.* 176 (1998) 536.
- [57] P. Burroughs, A. Hammett, A.F. Orchard, G.J. Thornton, *J. Chem. Soc. Dalton Trans.* 17 (1976) 1686.
- [58] J. Rynkowski, J. Farbotko, R. Touroude, L. Hilaire, *Appl. Catal. A: Gen.* 203 (2000) 335.
- [59] H. He, H.X. Dai, L.H. Ng, K.W. Wong, C.T. Au, *J. Catal.* 206 (2002) 1.
- [60] H. He, H.X. Dai, C.T. Au, *Catal. Today* 90 (2004) 245.
- [61] S. Ricote, G. Jacobs, M. Milling, Y. Ji, P.M. Patterson, B.H. Davis, *Appl. Catal. A: Gen.* 303 (2006) 35.
- [62] A.S. Ivanova, B.L. Moroz, E.M. Moroz, Y.V. Larichev, E.A. Paukshtis, V.I. Bukhtiyarov, *J. Solid State Chem.* 178 (2005) 3265.
- [63] L. Zhu, J.J. Yu, X.Z. Wang, *J. Hazard. Mater.* 140 (2007) 205.
- [64] A. Kotani, T. Jo, J.C. Parlebas, *Adv. Phys.* 37 (1988) 37.
- [65] J.S. Rieck, A.T. Bell, *J. Catal.* 96 (1985) 88.
- [66] Z.-Q. Zou, M. Meng, J.-Y. Luo, Y.-Q. Zha, Y.-N. Xie, T.-D. Hu, T. Lui, *J. Mol. Catal. A: Chem.* 249 (2006) 240.
- [67] G. Adachi, N. Iwanaka, *Chem. Rev.* 98 (1998) 1479.
- [68] M. Haneda, Y. Kintaichi, H. Hamada, *Phys. Chem. Chem. Phys.* 4 (2002) 3146.
- [69] J. Guo, S. Yuan, M. Gong, L. Zhang, D. Wu, M. Zhao, Y. Chen, *Acta Phys. Chim. Sin.* 23 (1) (2007) 73.
- [70] M. Boaro, M. Vicario, C. de Leinburg, G. Dolcetti, A. Trovarelli, *Catal. Today* 77 (2003) 407.

- [71] G.R. Rao, P. Fornasiero, R.D. Monte, J. Kašpar, G. Vlaic, G. Balducci, S. Meriani, G. Gubitosa, M. Graziani, *J. Catal.* 162 (1996) 1.
- [72] P. Fornasiero, R.D. Monte, G.R. Rao, J. Kašpar, S. Meriani, A. Trovarelli, M. Graziani, *J. Catal.* 151 (1995) 168.
- [73] X. Mo, J. Gao, N. Umnajkaseam, J.G. Goodwin Jr, *J. Catal.* 267 (2009) 167.
- [74] Z.-Y. Ma, C. Yang, W. Wei, W.-H. Li, Y.-H. Sun, *J. Mol. Catal. A: Chem.* 227 (2005) 119.
- [75] Y. Li, D. He, Q. Zhu, X. Zhang, B. Xu, *J. Catal.* 221 (2004) 584.
- [76] Y. Li, D. He, Z. Cheng, C. Su, J. Li, Q. Zhu, *J. Mol. Catal. A: Chem.* 175 (2001) 267.
- [77] W. Khaodee, B. Jongsomjit, S. Assabumrungrat, P. Praserttham, S. Godo, *Catal. Commun.* 8 (2007) 548.
- [78] F. Gaillard, *Catal. Lett.* 95 (2004) 23.
- [79] A. Trovarelli, C. De Letenbourg, G. Dolcetti, J.L. Lorca, *J. Catal.* 151 (1995) 111.
- [80] C. de Leitenburg, A. Trovarelli, J. Kašpar, *J. Catal.* 166 (1997) 98.
- [81] T. Jin, Y. Zhou, G.M. White, *J. Phys. Chem.* 91 (1987) 5931.
- [82] M. Luo, Y. Zhong, B. Zhu, X. Yuan, X. Zheng, *Appl. Surf. Sci.* 115 (1997) 185.
- [83] T. Ioannides, X.E. Verykios, *J. Catal.* 140 (1993) 353.
- [84] A.M. Efstathiou, *J. Mol. Catal.* 69 (1991) 41.
- [85] H.-T. Dai, J.-G. Duh, *J. Am. Ceram. Soc.* 73 (1990) 866.
- [86] C. Binet, M. Daturi, J.-C. Lavalley, *Catal. Today* 50 (1999) 207.
- [87] J.F. Múnera, S. Irusta, L.M. Cornaglia, E.A. Lombardo, D.V. Cesar, M. Schmal, *J. Catal.* 245 (2007) 25.
- [88] X.E. Verykios, *Int. J. Hydrogen Energy* 28 (2003) 1045.
- [89] C.M. Kalamaras, S. Americanou, A.M. Efstathiou, *J. Catal.* 279 (2011) 287.
- [90] C.M. Kalamaras, I.D. Gonzalez, R.M. Navarro, J.L.G. Fierro, A.M. Efstathiou, *J. Phys. Chem. C* 115 (2011) 11595.
- [91] A.A. Tsyganenko, V.N. Filimonov, *J. Mol. Struct.* 19 (1973) 576.
- [92] M.A. Henderson, *Surf. Sci. Rep.* 46 (2002) 1.
- [93] J. Ouyang, H. Yang, *J. Phys. Chem. C* 113 (2009) 6921.
- [94] M. Daturi, E. Finocchio, C. Binet, J.C. Lavalley, F. Fally, V. Perrichon, *J. Phys. Chem. B* 103 (1999) 4884.
- [95] A. Badri, C. Binet, J.-C. Lavalley, *J. Chem. Soc. Faraday Trans.* 92 (1996) 4669.
- [96] T. Onfroy, W.-C. Li, F. Schüth, H. Knözinger, *Phys. Chem. Chem. Phys.* 11 (2009) 3671.
- [97] M.I. Zaki, H. Knözinger, *Mater. Chem. Phys.* 17 (1987) 201.
- [98] K. Polychronopoulou, C.N. Costa, A.M. Efstathiou, *Catal. Today* 112 (2006) 89.
- [99] K. Polychronopoulou, A.M. Efstathiou, *Catal. Today* 116 (2006) 341.
- [100] K. Polychronopoulou, A. Bakandritsos, V. Tzitzios, J.L.G. Fierro, A.M. Efstathiou, *J. Catal.* 241 (2006) 132.
- [101] K. Tomishige, T. Miyazawa, M. Asadullah, S. Ito, K. Kumimori, *Green Chem.* 5 (2003) 399.
- [102] K. Tomishige, M. Asadullah, K. Kumimori, *Catal. Today* 89 (2004) 389.
- [103] M.M. Yung, W.S. Jablonski, K.A. Magrini-Bair, *Energy Fuel* 23 (2009) 1874.
- [104] D.K. Liguras, D.I. Kondarides, X.E. Verykios, *Appl. Catal. B: Environ.* 43 (2003) 345.
- [105] S. Cavallaro, V. Chiodo, S. Freni, N. Mondello, F. Frusteri, *Appl. Catal. A: Gen.* 249 (2003) 119.
- [106] A. Erdohelyi, J. Rasko, T. Kecskes, M. Toth, M. Domok, K. Baan, *Catal. Today* 116 (2006) 367.
- [107] M.C. Sánchez, R.M. Navarro, J.L. Fierro, *Int. J. Hydrogen Energy* 32 (2007) 1462.
- [108] T.G. Kuznetsova, V.A. Sadykov, S.A. Veniaminov, G.M. Alikina, E.M. Moroz, V.A. Rogov, O.N. Martynov, V.F. Yudanov, I.S. Abornev, S. Neophytides, *Catal. Today* 91 (2004) 161.
- [109] D.C. Grenoble, *J. Catal.* 51 (1978) 203.
- [110] D. Duprez, P. Pereira, A. Miloudi, R. Maurel, *J. Catal.* 75 (1982) 151.
- [111] Y. Denkwitz, A. Karpenko, V. Plzak, R. Leppelt, B. Schumacher, R.J. Behm, *J. Catal.* 246 (2007) 74.